Manipulation of Defect Formation in Semiconductor Nanocrystals for Photocatalysis and Magneto-optics

by

Wenhuan Lu

A thesis

presented to the University of Waterloo

in fulfillment of the

thesis requirement for the degree of

Master of Science

in

Chemistry (Nanotechnology)

Waterloo, Ontario, Canada, 2020

Author's Declaration

I hereby declare that I am the sole author of this thesis. This is a true copy of the thesis, including any required final revisions, as accepted by my examiners.

I understand that my thesis may be made electronically available to the public.

Abstract

Defects play a significant role in semiconductor nanocrystals (NCs) as they can influence their electrical and optical properties via vacancy doping or aliovalent doping. Localized surface plasmon resonance (LSPR), the phenomenon of collective oscillation of free electrons, allows for degenerately doped metal oxide NCs to be used as infrared plasmonic materials with promising applications in photovoltaics, sensing, electrochemistry photocatalysis and magneto-optics.

In this study, sub-stoichiometric WO_{3-x} NCs were used for plasmon-induced photodegradation of rhodamine-590 (Rh-590), with the advantages of facile synthetic method and simple configuration, as well as the potential to efficiently absorb NIR to MIR portion of solar radiation relative to the typical single-phase semiconductor and heterostructured photocatalysts reported. WO_{3-x} NCs exhibit enhanced photocatalytic activity in contrast to bulk stoichiometric WO_3 and sub-stoichiometric $WO_{2.9}$ powders as well as annealed WO_{3-x} NCs with nearly complete Rh-590 degradation (97.8%) within 2 hours in the dark at 20 ℃. Photocatalytic performance of WO_{3-x} NCs increases with temperature because the wavelength of the blackbody radiation approaches to LSPR peak maximum. The WO_{3-x} NCs show good recyclability with degradation percentage of ca. 82.6% after 3 cycles at 30 ℃. Scavengers were used to study the mechanism of photocatalytic degradation by WO_{3-x}, suggesting that reactive radicals (O_2^- and OH·) make significant contribution to Rh-590 photodegradation. The results of this work demonstrate the important role of LSPR-associated free electrons in single-phase plasmonic semiconductor NCs for efficient photodegradation of dyes.

Additionally, the single-phase plasmonic semiconductor NCs have emerged as promising materials for carrier polarization as magneto-optical materials. ZnO NCs, as an environmentally benign, cost effective material with abundant availability and reduced toxicity, are proposed as a model system to systematically investigate the effect of defect formation on plasmonic properties and charge carrier polarization in the presence of an external magnetic field. The defect concentration, responsible for plasmonic properties, was manipulated via changing synthesis conditions and doping with Mg ions and evaluated with the help of photoluminescence (PL) spectroscopy. Importantly, the Curie-type decay associated with unpaired localized electrons can also be manipulated by controlling defect concentration as indicated by magnetic circular dichroism (MCD) spectra. The defect-correlated band splitting monitored by MCD spectroscopy in Mg-doped ZnO NCs would be an intriguing topic for further study. The ability to control exciton polarization in pure (undoped) ZnO NCs using individual electrons localized on point defects enable the potential technological applications including spintronics and quantum information processing.

Acknowledgements

I would like to express my gratitude to my supervisor Dr. Pavle Radovanovic for his guidance and encouragement in my research. He has provided me with valuable advice in every stage of my project to help me overcome the difficulties, and has been very patient and supportive during my graduate study. I would also like to thank my advisory committee members, Dr. Vivek Maheshwari and Dr. Holger Kleinke for all the help and assistance as well as taking time to read my thesis and attend my defence.

I would like to thank Cathy Van Esch for kindly answering all my questions. I thank Dr. Carmen Andrei at the Canadian Center for Electron Microscopy for her assistance in TEM image collection. I also thank Dr. Holger Kleinke's group and Dr. Linda Narzar's group for the help with XRD collection and FTIR measurements.

My sincere thanks will extend to my past and current group members, Penghui Yin, Yufeng Zhou, Natalie Garnet, Vahid Ghodsi, Susi Jin, Yunyan Wang, Paul Stanish, Yi Tan, Shuoyuan Chen, Nathaniel Smith, Chenwei Zhang, I-hsuan Yeh, Archisman Ray and Khue Nguyen. They kindly gave me great suggestions and shared their experience with me, which is a huge support during my graduate study. Specifically, I would like to thank Penghui for kindly answering all my questions, being available and supportive to help, and Natalie for all the help and encouragement.

Finally, I am very grateful to my parents, my sister, my boyfriend and all my friends for being supportive and available to help all the time regardless of time difference and long distance.

Table of Contents

List of Figures

List of Tables

List of Abbreviations

Acac	Acetylacetonate
AQY	Apparent Quantum Yield
AZO	Aluminum-doped Zinc Oxide
DDOL	1-Dodecanol
DMSs	Diluted Magnetic Semiconductors
DMSO	Diluted Magnetic Semiconductor Oxides
EDX	Energy Dispersive X-ray
FIR	Far-Infrared
FTIR	Fourier Transform Infrared Spectroscopy
FWHM	Full Width of Half Maximum
HER	Hydrogen Evolution Reaction
HNC	Heterostructured NCs
ICO	Indium-doped Cadmium Oxide
ITO	Indium-doped Tin Oxide
LSPR	Localized Surface Plasmon Resonance
MCD	Magnetic Circular Dichroism
MIR	Mid-Infrared
NCs	Nanocrystals
NHE	Standard Hydrogen Electrode
NIR	Near-Infrared

NPs	Nanoparticles
NWs	Nanowires
ODE	1-Octadecene
PEC	Photoelectrochemical cell
PL	Photoluminescence
QD	Quantum dot
SER	Surface Enhanced Raman
TEM	Transmission Electron Microscopy
UPS	Ultraviolet Photoelectron Spectroscopy
UV-Vis	Ultraviolet-Visible- Spectroscopy

Chapter 1

Introduction

1.1 Localized surface plasmon resonance

Plasmonic nanocrystals (NCs) have been researched intensively during the past decades as emerging materials with remarkable optical properties for photovoltaics,[1] photocatalysis[2] and biosensing.[3] Localized surface plasmon resonances (LSPRs) are the collective oscillations of free electrons on the surface of nanoparticles (NPs) when irradiated with incident light possessing the resonant frequency of electrons oscillations (Figure 1.1).[4] Originally, LSPRs were thought to be specific only to metallic nanostructures and enormous work has been done in noble metal NPs, especially gold (Au) and silver (Ag) with the resonant frequencies lying in the visible spectral range.[5] After LSPRs in these noble metals have been well established, the manifestation of metal-like LSPRs in a variety of degenerate semiconductor NCs including both n-type and p-type semiconductors opened up a new field in the study of plasmonics.[6]
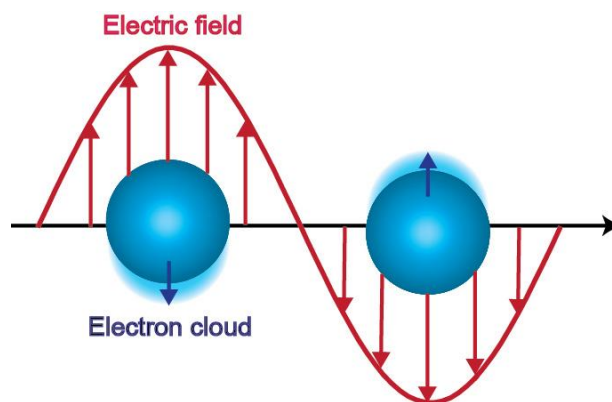
Figure 1.1 Illustration of the excitation of the LSPRs of a spherical nanoparticle by incident electromagnetic radiation.

Generally, the metal oxides including zinc oxide (ZnO),[7] tungsten oxide (WO$_3$),[8] cadmium oxide (CdO),[9] and indium oxide (In$_2$O$_3$)[10,11] are n-type plasmonic semiconductor NCs due to the oxygen vacancies or aliovalent doping, whereas the chalcogenides including copper sulfide (Cu$_{2-x}$S), copper selenide (Cu$_{2-x}$Se), and copper telluride (Cu$_{2-x}$Te) are p-type plasmonic semiconductor NCs due to the copper vacancies.[12] These plasmonic NCs can support LSPRs in the near-infrared (NIR) to mid-infrared (MIR) region (Figure 1.2) due to relatively small free carrier concentration compared to metal nanostructures.[5] Similar to noble metals, LSPR frequency of semiconductor nanocrystals can be tuned by size,[13] shape,[9] composition[14] and dielectric environment[15] of nanoparticles. Besides these, semiconductor NCs offer a unique opportunity to tune LSPR frequency via adjusting the type and concentration of charge carriers by intrinsic or extrinsic doping.[5]
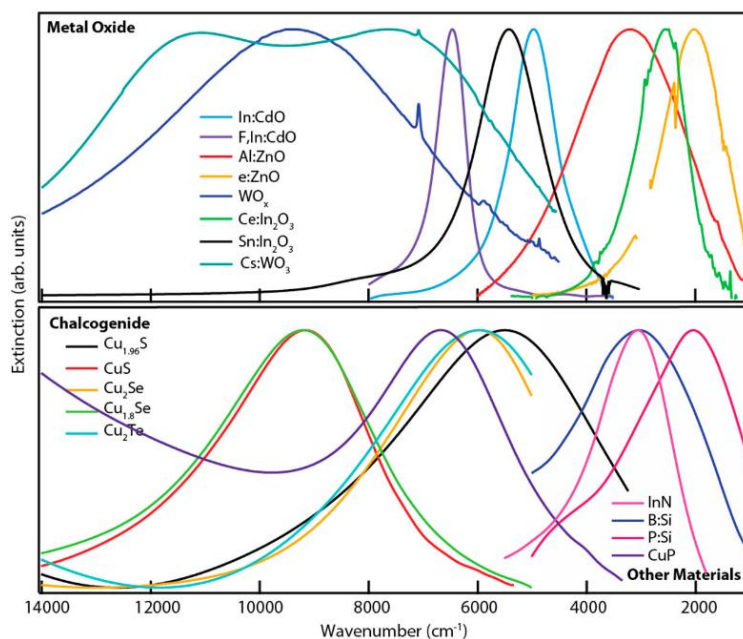
Figure 1.2 LSPR in different semiconductor NCs.[5] Reproduced with permission from ref 5. Copyright 2018 American Chemical Society.

1.1.1 Generating LSPR in semiconductor nanocrystals

To achieve LSPR in metal oxide semiconductors, there are two strategies including intrinsic doping (self-doping: e.g. vacancy doping) and extrinsic doping. Some metal oxides like In_2O_3 and ZnO are naturally n-type semiconductors with a certain amount of oxygen vacancies, hence, in an intrinsically doped system, an oxygen vacancy ($V_O^{\cdot\cdot}$) can create a shallow donor level, introducing two "extra" electrons to the conduction band (Figure 1.3b).[16] In sub-stoichiometric tungsten oxide (WO_{3-x})[8] and molybdenum oxide (MoO_{3-x}) NCs,[17] the free electrons introduced by these oxygen vacancies are sufficient to achieve LSPR in the NIR range and the resultant LSPR peak can be blue shifted with higher concentration of oxygen

3

vacancies.[18] In extrinsically doped system such as tin doped indium oxide (ITO)[19], indium doped cadmium oxide (ICO)[9] and aluminum doped zinc oxide (AZO)[7], the increased carrier concentration mainly originates from substitutional doping (Figure 1.3c). In this case shallow donor or acceptor levels are introduced into the band structure by substituting a fraction of host lattice cations with dopants having higher or lower valence state.[16]

The increased charge carrier concentration in conduction band leads to an increased apparent optical bandgap which is defined as the energy difference between the highest occupied state in the conduction band and the top of the valence band for n-type semiconductors, or the energy difference between the bottom of the conduction band and the highest occupied state in the valence band for p-type semiconductors. Figure 1.4 illustrates examples for each type. For AZO NCs the bottom of the conduction band is occupied by electrons from higher valence state dopants, thus the optical bandgap is increased. In the case of $Cu_{2-x}S$, the "extra" holes introduced by copper vacancies can decrease the highest energy levels of the valence band. The decreased valence band is lower than it would be in undoped materials, also leading to an increase of the optical bandgap. This is known as the Burstein-Moss effect.[20]
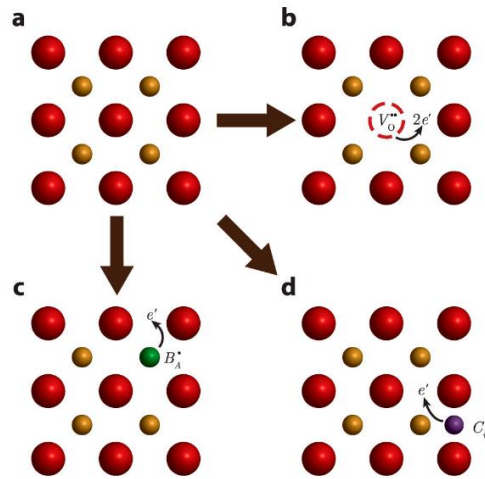
Figure 1.3 Schematic representation of the common doping mechanisms in metal oxides relative to (a) a basic lattice containing metal cations (orange spheres) and oxygen anions (red spheres). (b) oxygen vacancies act as double electron donors, (c) aliovalent substitutional impurities and (d) interstitial impurities typically contribute one free electron.[16] Reproduced with permission from ref 16. Copyright 2014 American Chemical Society.
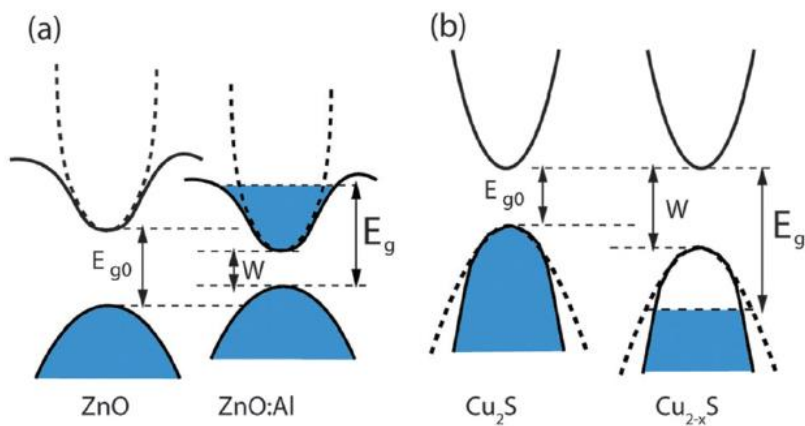
Figure 1.4 Band structures of plasmonic semiconductor nanoparticles. (a) The intrinsic bandgap (W) of AZO is smaller than that of undoped zinc oxide (E_{g0}), but the optical bandgap

(E_g) is increased, due to the state filling effect (Burstein-Moss effect) (b) Both intrinsic and optical bandgaps become larger when the doping level is increased in self-doped copper sulfide.[20] Reproduced with permission from ref 19. Copyright 2014 The Royal Society of Chemistry.

1.1.2 Drude model of free electron gas

As aforementioned, the concept of LSPR corresponds to the collective oscillations of free electrons on the surface of NPs, consequently, a strong electromagnetic field is generated leading to a charge separation and enhanced light absorption/scattering at the resonance wavelength.[21] Upon excitation with external incident light, the charge distribution inside a NP is determined by several components of the dielectric function, including electronic effects from interband or intraband excitation ($\epsilon_{electronic}$), atomic effects from vibrational or phonon excitation (ϵ_{atomic}) as well as conduction hole or electron excitations ($\epsilon_{conduction}$). The dielectric function or polarizability is an additive property and expressed as following:

$$\epsilon = \epsilon_{electronic}(\omega) + \epsilon_{atomic}(\omega) + \epsilon_{conduction}(\omega) \tag{1.1}$$

The light matter interaction is determined by the overall dielectric properties, however, only optical properties resulting from conduction component of dielectric function will be discussed due to the correlation between free carrier concentration and LSPR frequency.[5] The relationship between them can be described using the Drude-Lorenz model based on the assumption that the free electron in a material can be described by an effective mass m^* and a charge $-e$ and that the material is considered as a "gas" of free carriers (ε_b=1). The dielectric

function determining the optical properties of the plasmonic material in the applied Drude model is a complex function,[22,23] where:

$$\varepsilon_m = \varepsilon_b[1 - \frac{\omega_p^2}{\omega(\omega+i\gamma)}] \tag{1.2}$$

$$\omega_p = \sqrt{\frac{e^2 N}{m^* \varepsilon_0}} \tag{1.3}$$

When defined to nanoparticles, the Equation (3) is modified to:[24]

$$\omega_{LSPR} = \sqrt{\frac{\omega_p^2}{1+2\varepsilon_m} - \gamma^2} \tag{1.4}$$

where ε_b is the background permittivity from the bound electrons in the crystals. ε_0 is the permittivity of free space, ε_m is dielectric constant of the surrounding medium, ω_p is the bulk plasma frequency, N is free carrier concentration, m^* is the free carrier effective mass, γ is a LSPR peak-broadening factor (damping constant) based on the total carrier scattering frequency.[22–24]

The absorption coefficient is linearly dependent on N:[11]

$$A = \frac{Ne^2}{m^* \varepsilon_0 nc\tau\omega^2} \tag{1.5}$$

where τ is the relaxation (damping) time and c is the speed of light, n is refractive index.

According to Equation 1.3, it is evident that the plasma frequency is directly proportional to the square root of the free carrier concentration suggesting LSPR peak can be shifted by controlling the free carrier concentration. Bulk noble metals like silver and gold have fixed free carrier concentrations in the range of 10^{23} cm^{-3} with LSPR spectrum lying in the visible to ultraviolet (UV) region.[23] Unlike noble metals, the free carrier concentration of degenerately

doped semiconductors can be adjusted by various doping level, and the absorption features arising from the LSPR can be tuned to NIR and MIR region.[25] Luther *et al*. calculated the LSPR frequency dependence on free carrier concentration and doping constraints in quantum dots (QD) (Figure 1.5).[15] Doping concentrations with 10^{16}-10^{18} cm^{-3} would achieve LSPRs in the THz regime, while carrier concentrations of 10^{19}-10^{22} cm^{-3} would obtain LSPRs in the NIR, MIR and even far-infrared (FIR) regions.
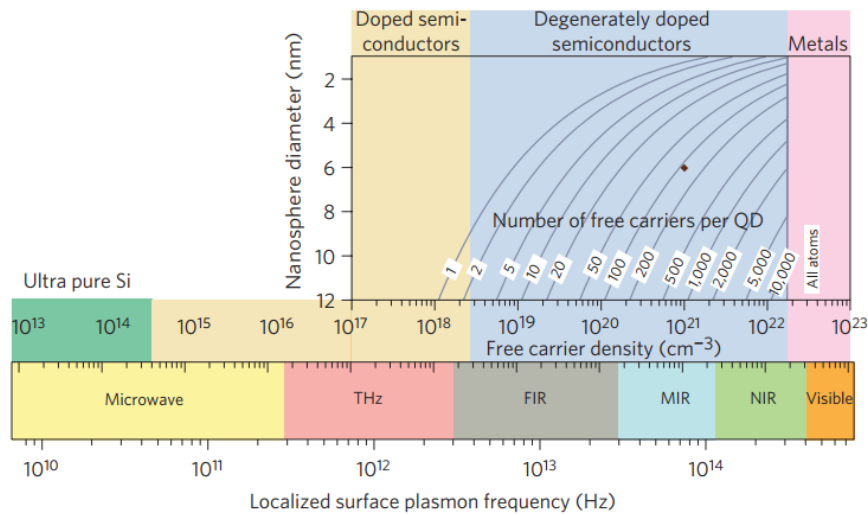
Figure 1.5. Localized surface resonance plasmon (LSPR) frequency dependence on free carrier concentration and doping constraints in quantum dots (QD).[15] Reproduced with permission from ref 15. Copyright 2011 Nature.

The damping constant in Equation 1.4 describes the damping of the collective oscillations of the carriers based on total scattering frequency, which is important for understanding the energy loss from an excited LSPR. There are several scattering mechanisms including electron-electron scattering (γ_{e-e}), electron-phonon scattering (γ_{e-ph}), interband transition scattering

(γ_{ib}), surface scattering (γ_s), electron-impurity scattering (γ_{e-i}) as well as material-specific and morphology-specific scattering mechanisms. These scattering mechanisms are additive via Matthiessen's rule, and the resultant overall scattering function is:

$$\gamma = \sum \gamma_i = \gamma_{e-e} + \gamma_{e-ph} + \gamma_{ib} + \gamma_s + \gamma_{e-i} + \gamma \dots \qquad (1.6)$$

Among different scattering mechanisms, electron-electron scattering has only a minor contribution because of the minimal interaction between electrons. Electron-phonon scattering strongly depends on temperature and has a significant effect on overall scattering only at high temperatures. In terms of interband transition scattering, since semiconductors have little overlap between intra- or inter-band excitation and free carrier excitation, it does not have strong influence on the LSPR excitation. When the sizes of NCs are less than the electron mean free path, surface scattering can contribute significantly to the damping. The most important source of damping is defect scattering originated from the impurities and vacancies in semiconductors.[5,18] In absorption spectra, the damping constant is indirectly correlated to the width of the LSPR peak (the higher damping, the broader the resonance) and the quality factor of LSPR mode which is the ratio of the LSPR peak energy and the full width at half maximum (FWHM) of the resonance peak.[26] The higher quality factor, the stronger plasmonic response. In summary, the optical properties of plasmonic semiconductors are dependent on the free carrier concentration and overall free carrier scattering.

1.2 Plasmonic photocatalysis

With global industrialization and population growth, the typical energy resources such as coal and petroleum products have been largely consumed. The research and utilization of

sustainable energy have become the focus of world attention. Solar energy is the most abundant renewable energy source which has been utilized and converted into chemical/ electricity/thermal energy in the application of photocatalysis, photovoltaic devices and energy-efficient windows. In 1972, Fujishima and Honda[27] used TiO_2 as electrode for the electrochemical photolysis of water, which effectively introduced semiconductor photocatalysis for environmental remediation and solar energy conversion.

Water pollution, as a major environmental problem, is getting severe due to the rapid development of industries. The increasing number of contaminants including heavy metals, micropollutants and organic compounds released in water leads to the shortage of fresh water. The utilization of photocatalysis to degrade these contaminants plays an essential part to purify the polluted water or wastewater. Take the dyes released from textile or paper industries as an example, they are generally toxic and difficult to destroy. However, with the help of photocatalytic degradation, these organic pollutants are decomposed to small molecules (CO_2, H_2O, and NH_3), which are not particularly toxic. In a typical photocatalytic reaction (Figure 1.6a), photogenerated electrons reduce adsorbed oxygen (O_2) to produce superoxide (O_2^-) radicals which will further form hydroxyl radicals (OH·), while photogenerated holes react with H_2O to form OH· radicals. The resultant hydroxyl radicals contribute to the mineralization and degradation by oxidizing the organic pollutants.[28]
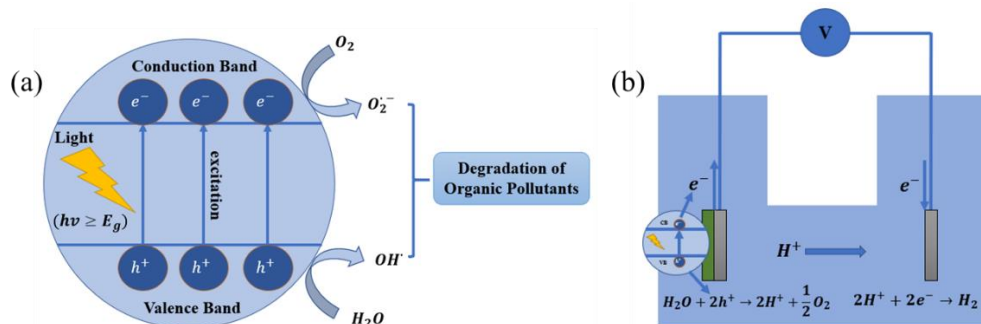
Figure 1.6 (a) The mechanism of general semiconductor photocatalysis,[29] (b) Schematic diagram of a photo-electrochemical cell and related reactions.[30]

The photoelectrochemical (PEC) splitting of water is an efficient approach to convert solar energy into chemical energy, which is promising strategy for the development of sustainable energy in the future. In the photo-electrochemical cell introduced by Fujishima and Honda, the electron-hole pairs are generated upon light irradiation on the photo-anode, where O_2 and H^+ are produced through the oxidation of water by photo-generated holes, whereas the H_2 is generated on the cathode through the reduction of H^+ by the transfer of photo-generated electrons along the external circuit (Figure 1.6b).[30] The produced H_2 is regarded as a potential "green" energy source due to high energy generation, zero pollutant production and facile storage. To make water splitting work, the bandgap energy of the semiconductor photocatalyst needs to straddle the range between the reduction potential of H^+ and the oxidation potential of H_2O for generation of H_2 and O_2. The energy band positions of the commonly used efficient photocatalysts and work functions of noble metals are illustrated in Figure 1.7.

11

E(eV)
0

Semiconductor photocatalysts   Noble metals

E(SHE)
Redox groups
-1

-4.0

3.0 eV   2.6 eV   2.4 eV

Ag (-4.7 eV)   0
Au (-5.1 eV)
Pd (-5.2 eV)   +1

O_2/O_2^- (-0.28 eV)
H_2/H^+ (0 eV)
O_2/OH^- (+0.4 eV)
O_2/H_2O_2 (+0.68 eV)
Ag/Ag^+ (0.80 eV)
O_2/H_2O (+1.23 eV)

-5.0

1.7 eV   3.2 eV   2.5 eV

-6.0

3.2 eV   3.2 eV   2.8 eV

CdSe

CdS   AgCl   AgBr   AgI

Pt (-6.3 eV)   +2

Au/Au^+ (1.83 eV)

-7.0

TiO_2 ZnO Bi_2O_3 WO_3

$AgCl + e^- \Leftrightarrow Ag + Cl^- + 0.22$ eV   +3
$AgBr + e^- \Leftrightarrow Ag + Br^- + 0.07$ eV
$AgI + e^- \Leftrightarrow Ag + I^- - 0.15$ eV

-8.0
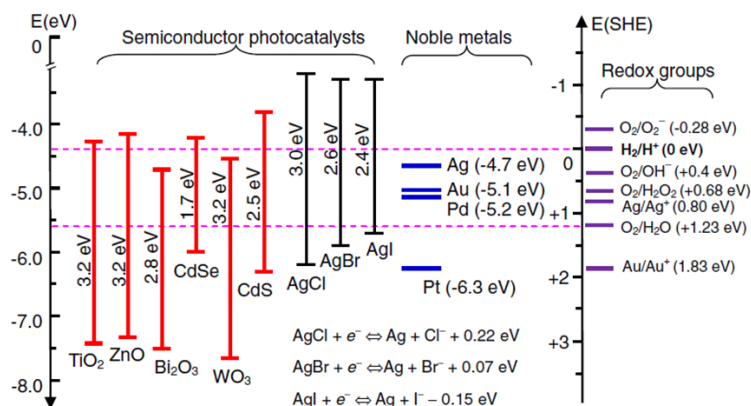
Figure 1.7 Energy band positions of common materials in photocatalysis, including the conduction and valence bands of the semiconductor photocatalysts, the work functions of the noble metals, and the electrochemical potentials of redox groups.[31] Reproduced with permission from ref 30. Copyright 2013 IOP Publishing.

After Fujishima and Honda's work[27], semiconductor photocatalysis has emerged as a very promising method for the harvesting and conversion of solar energy during the last few decades. However, the major obstacles to optimal photocatalytic performance of many promising metal oxide semiconductors, such as ZnO and TiO_2, is the recombination of photo-generated free carriers, and a limited absorption of the solar spectrum due to their wide band gaps. The solar spectrum contains only 5-7 % of UV light, while the contributions of visible and IR radiation to the solar spectrum are 46 % and 47 %, respectively. The plasma frequency for semiconductors is usually in the visible to IR region, indicating that plasmonic photocatalysis can utilize the sun light more efficiently. Additionally, the "hot electrons" generated by plasmon oscillations in semiconductor nanostructures can play an active role in the

photocatalytic reactions. Plasmonic NCs have consequently been used in photocatalysis involving different system configurations reported in literature based on different mechanisms.

1.2.1 Plasmonic noble metal-semiconductor heterostructure

Since LSPRs in noble metals have been well established at present, like Au and Ag NCs with plasmonic resonant frequencies lying in the visible range, heterojunction-based photocatalysts or photoelectrodes involving plasmonic noble metal and semiconductor NCs have been explored extensively as an alternative solution to the insufficient spectral absorption of semiconductor photocatalysts. The photocatalytic activity can be significantly enhanced by plasmonic energy transfer from noble metal to semiconductor based on three major mechanisms including light scattering/trapping, plasmon-induced resonance energy transfer (PIRET) and hot electron injection.[32]

In light scattering/trapping mechanism, a metal-semiconductor heterojunction is formed by integrating large plasmonic metal nanoparticles and semiconductors. The incident light can be scattered by the metal nanoparticles to penetrate the semiconductor, leading to an increase in photon flux in the semiconductor (Figure 1.8a). It is also called "light trapping" as this scattering effect enhances the light absorption and charge separation in the active semiconductor component. For FIRET mechanism, the excitation of plasmon in metal NCs can generate a strong dipole allowing the plasmonic energy in the metal to transfer non-radiatively to the semiconductor via near field dipole-dipole interaction, generating electron-hole pairs in the semiconductor (Figure 1.8b). Hot electron injection mechanism has been commonly used in heterostructured photocatalysts. In the noble metal-semiconductor

13

heterostructure, the energy of "hot carriers" generated by plasmonic noble metals via Landau damping are higher than the Schottky barrier at the metal-semiconductor interface. Therefore, these "hot carriers" can be directly injected into the conduction band of the semiconductor for the redox reactions (Figure 1.8c).
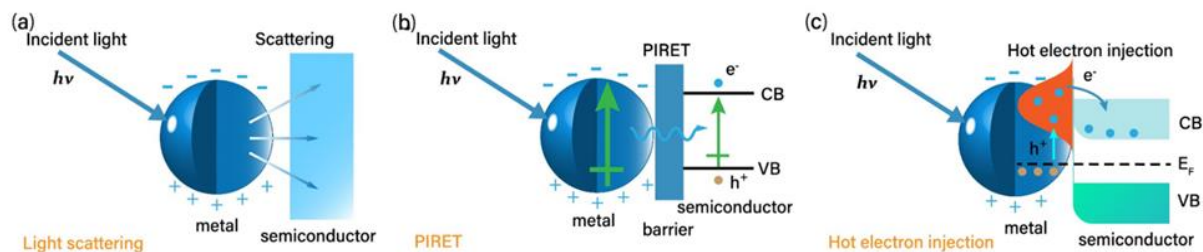
Figure 1.8 Three mechanisms of plasmonic energy transfer from a plasmonic metal to a semiconductor. (a) Light scattering; (b) PIRET; (c) Hot electron injection.[32] Reproduced with permission from ref 31. Copyright 2017 The Royal Society of Chemistry.

Awazu et al.[33] demonstrated a TiO_2/Ag heterostructure for enhanced photocatalytic decomposition of methylene blue under near UV illumination due to the enhanced electric field amplitude on the surface of plasmonic Ag NPs. In their work, a silica (SiO_2) shell was used to cover Ag NPs to prevent oxidation of Ag by direct contact with TiO_2. The enhancement of the photocatalytic activity increases with a decreased thickness of the SiO_2 shell.[33] Another example is the utilization of the heterostructure comprising gold nanoparticles supported on P25 titania (Au/TiO_2) in photocatalytic water splitting under UV and visible light. The comparison of hydrogen evolution upon 532 nm laser irradiation (close to the plasmonic peak of Au NPs at 550 nm) between Au (1.5 wt%) and TiO_2 indicates that there is no photocatalytic activity for TiO_2 itself but a significantly enhanced activity for Au (1.5 wt%)/TiO_2. The

proposed mechanism is that the generated electrons in plasmonic Au NPs are injected into the TiO$_2$ conduction band and the generated holes in the Au NPs are quenched by sacrificial electron donor, ethylenediaminetetraacetic acid (EDTA). So the electrons in the TiO$_2$ conduction band can activate the hydrogen generation process.[34]

The plasmonic noble metal/semiconductor heterostructure are proved to exhibit enhanced photocatalytic performance and more efficient utilization of the natural light. However, one of the main concerns about this type of heterostructure is the high cost of noble metals can hinder the large-scale applications as photocatalysts.

1.2.2 Plasmonic non-noble metal heterostructure

The heterostructures containing plasmonic semiconductor NCs have become an attractive field of research due to the high cost of noble metals in the noble metal/semiconductor heterostructures. Lian et al.[35] reported CdS/Cu$_7$S$_4$ heterostructured nanocrystals (HNCs), with Cu$_7$S$_4$ as the plasmonic component, for photocatalytic H$_2$ evolution upon irradiation with IR light (up to 2500 nm).[35] CdS/Cu$_7$S$_4$ HNCs exhibit high performance with the average H$_2$ evolution rate of 14.7 $\mu mol \cdot h^{-1} \cdot g^{-1}$, whereas the Cu$_7S_4$ NCs and the mixture of Cu$_7$S$_4$ NCs and CdS NCs have no H$_2$ evolution activity (Figure 1.9a). The apparent quantum yields (AQYs) for the hydrogen evolution reaction obtained using monochromic light with different wavelengths is in good agreement with LSPR spectrum (Figure 1.9b). Taken together these results indicate that hydrogen evolution activity comes from the LSPR-excited carrier transfer from Cu$_7$S$_4$ to CdS phase. Transient absorption (TA) measurements revealed the mechanism

(Figure 1.9c), where both hot-electron injection and ultralong-lived charge separation (>273 μs) at the p-n heterojunction of the HNCs contribute to the high catalytic activity.[35]

Besides p-type plasmonic semiconductor like Cu_7S_4, n-type plasmonic semiconductor have also been considered in heterostructured photocatalysts. Zhang et al.[36] demonstrated a $W_{18}O_{49}$/g-C_3N_4 heterostructure which is photocatalytically active throughout the solar spectrum (UV, vis, NIR region) (Figure 1.9d-f). The Z-scheme energy band configuration allows for charge carrier separation and plasmon-induced hot electron injection process, leading to the highly efficient H_2 evolution (Figure 1.9g).[36]

Although different heterostructured photocatalytic systems involving nanoscale plasmonic semiconductors have been shown promise for hydrogen evolution and other reactions relevant to long-term sustainability in the proof-of-concept laboratory experiments, they generally suffer from the complexity of the design and preparation, and it is, therefore, challenging to implement them commercially.
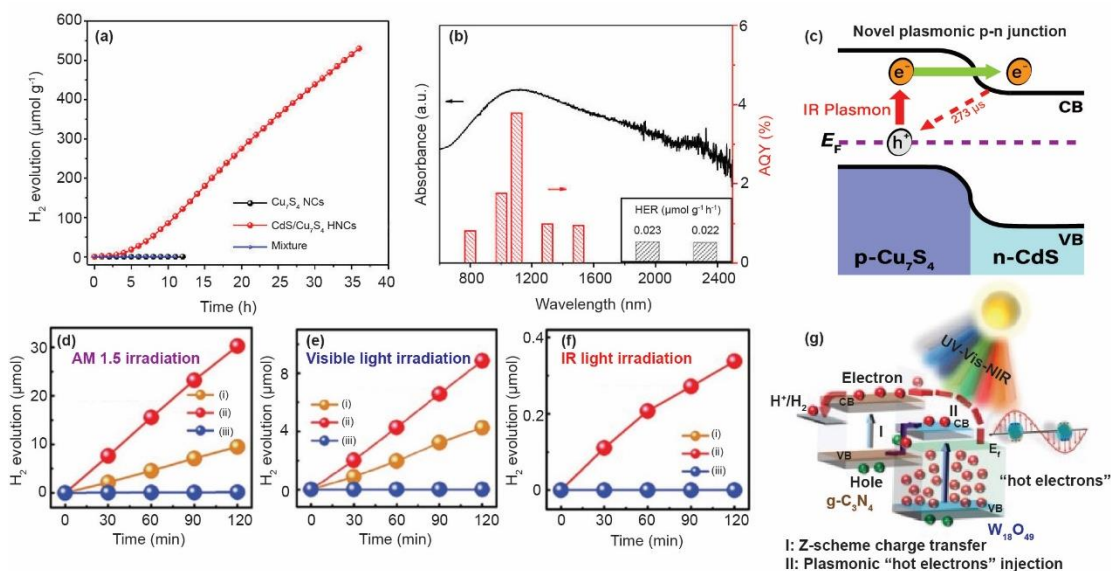
Figure 1.9 (a) Temporal photocatalytic H_2 evolution over Cu_7S_4 NCs, CdS/Cu_7S_4 HNCs and a mixture of Cu_7S_4 NCs and CdS NCs under IR illumination ($\lambda > 800$ nm) in a Na_2S-Na_2SO_3 aqueous solution. (b) Absorption spectrum and AQY for HER of the CdS/Cu_7S_4 HNCs under the monochromic light (6 mW cm^{-2}). (c) Hot-electron injection at the plasmonic p-n heterojunction upon IR light-plasmon excitation.[35] (d) simulated sunlight irradiation, (e) visible-light irradiation, and (f) IR-light irradiation: i) g-C_3N_4 nanosheets, ii) $W_{18}O_{49}$/g-C_3N_4 heterostructure, and iii) $W_{18}O_{49}$ nanograsses. (g) Energy band configuration and photoinduced charge-carriers generation/transfer process in the nonmetal plasmonic Z-scheme photocatalyst with the $W_{18}O_{49}$/g-C_3N_4 heterostructure under UV-vis-NIR light excitation.[36] Reproduced with permission from ref 34, 35. Copyright 2019 American Chemical Society. Copyright 2017 Wiley-VCH.

17

1.2.3 Single-phase semiconductor nanocrystals

In contrast to heterostructured photocatalysts, single-phase plasmonic semiconductor NCs can be prepared by facile synthetic methods and have simple configuration. Additionally, they have the potential to efficiently absorb NIR to MIR portion of solar radiation and enhance photocatalytic activity. A recent study of the photocatalytic activity of $Cu_{2-x}Se$ NCs has suggested the plasmon-driven dimerization of 4-nitrobenzenethiol (NBT) to 4, 4′-dimercaptoazobenzene (DMAB) on NC surface (Figure 1.10a) with a yield comparable to those observed from noble metal nanoparticles.[37] The resulting DMAB has been detected by surface enhanced Raman spectroscopy upon irradiation of NCs at 1035 nm (Figure 1.10b).[26] Although $Cu_{2-x}Se$ is a p-type plasmonic semiconductor, the authors suggest that the electrons of the initially formed hot electron-hole pairs have sufficient energy to drive the dimerization reactions, if the hot holes are scavenged by appropriate reductants like oxygen dissolved in the solvent.[37]

Photocatalytic activity of n-type plasmonic semiconductor nanostructures have also been investigated. Paik et al.[38] have demonstrated the stable photocatalytic hydrogen production using sub-stoichiometric WO_{3-x} nanowires (NWs) under UV/vis light irradiation in the presence of alcohol as a sacrificial agent. As a result of the conduction band population with free electrons introduced by oxygen vacancies, the apparent optical band gap is increased in these WO_{3-x} NWs. Therefore, the lowest unoccupied conduction band states become more negative than the standard hydrogen reduction potential, in contrast to bulk WO_3 (Figure 1.10c).[38] Figure 1.10d illustrates the H_2 evolution from platinized plasmonic WO_{3-x} NWs. On

the other hand, stoichiometric platinized WO_3 exhibits no activity toward H_2 evolution attesting to the critical role of the conduction band position relative to the H_2 reduction potential. Although LSPR of WO_{3-x} NWs is not directly involved in the H_2 evolution in this work, the photocatalytic activity is enabled by the Burstein Moss effect which is a key property of plasmonic semiconductor NCs. Sub-stoichiometric WO_{3-x} NWs still have the great potential to provide efficient plasmonic photocatalytic activity due to the large bandgap energy and plasmonic properties originating from the oxygen deficiencies. Although the studies on using plasmonic semiconductor NCs in solar energy harvesting and conversion are just beginning to emerge, they are likely to provide important new opportunities in the field of photocatalysis and environmental remediation.
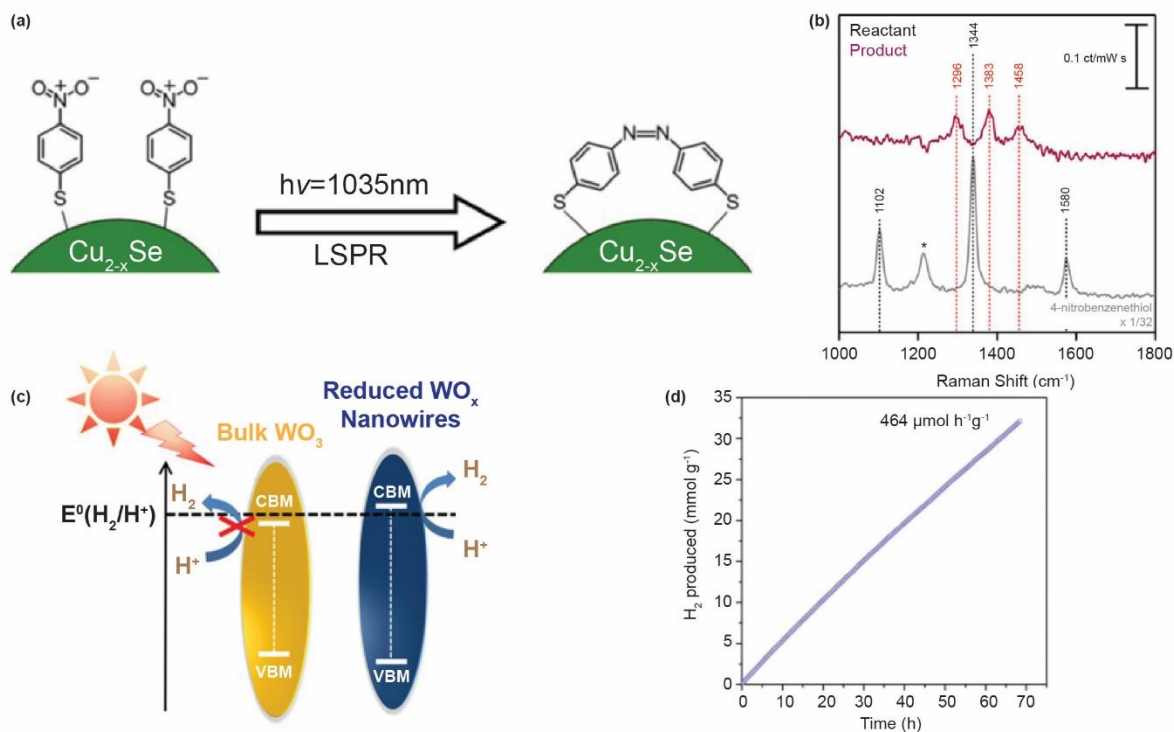
Figure 1.10 (a) Simplified depiction of plasmon-driven chemical conversion from 4-NBT to DMAB, (b) SER difference spectrum of oleylamine-capped $Cu_{2-x}Se$ NPs (maroon), shows the plasmon-driven dimerization of the reactant 4-nitrobenzenethiol (black dashed lines) to the product, 4,4′-dimercaptoazobenzene (red dashed lines). Light gray spectrum shows the normal Raman spectrum for NBT.[37] (c) Energy levels of bulk WO_3 and WO_x calculated by UPS results and the optical band gap. (d) Hydrogen evolution over time from 1 wt % Pt-loaded WO_x NWs under UV/vis light illumination (150 W Hg-Xe arc lamp) in 1:1 vol. mixtures of $MeOH/H_2O$.[38] Reproduced with permission from ref 36, 37. Copyright 2019 American Chemical Society. Copyright 2018 American Chemical Society.

1.3 Magneto-optics

1.3.1 Magnetic semiconductors

Dilute magnetic semiconductors (DMSs) are an important class of materials for application of spintronics because they can make use of electron charge and spin properties in semiconductors. DMSs are formed by doping magnetic elements (usually transition metals) into non-magnetic semiconductors, imparting magnetic behavior to the host material through exchange interaction between the s or p electrons of the host lattice and the d-electrons from the magnetic impurities.[39,40] The motivation behind research in DMSs is to create useful semiconductors with Curie temperature of at least 500 K for application in room-temperature electronic devices.[41] The diluted magnetic semiconductor oxides (DMSOs) usually use transition metal doped wide-bandgap metal oxides, including Ni- and Co-doped ZnO,[42,43] Co-doped TiO_2,[44] and Ni-doped SnO_2,[45,46] Cr- and Mn-doped In_2O_3,[47,48] which have been investigated for high-temperature ferromagnetism.

The mechanism of magnetic interactions with DMSO materials is still under debate. However, the magnetic behavior in DMSOs has often been attributed to the presence of dopants and defects within the lattice (ie. oxygen vacancies). According to the first-principles calculations from Hu et al.[49] oxygen vacancies can induce ferromagnetism in Fe-doped In_2O_3 with the prediction that the long range ferromagnetic ordering can be established by introducing enough dopants and oxygen vacancies. In the bound magnetic polaron model, the magnetic polaron is formed by the electrons in the shallow donor states like oxygen vacancies. The exchange interactions between dopant electrons are mediated by spin polarized charge

carriers which are trapped in defect bands. As the density of defects increases, the magnetic

polaron overlaps leading to spin-split of impurity bands. High Curie temperatures are attributed

to the hybridization and charge transfer from a donor-derived impurity band to unoccupied 3d

states at the Fermi level.[41] Given the correlation between magnetic behavior and defects, the

manipulation of oxygen vacancies through controlling sample synthesis method is often

associated with observed magnetic properties.[50]

1.3.2 Plasmonic semiconductors

Nanosystems combining magnetic and plasmonic functionalities have attracted broad

attention in recent years.[51] The magneto-optical response of these systems can be significantly

increased due to the electromagnetic field enhancement associated with LSPR. Simultaneously,

the control of plasmonic properties by an external magnetic field can be achieved, which allows

the development of plasmonic devices.[52] By exploring IR magneto-optical responses arising

from the doped semiconductor NCs with LSPRs, Schimpf et al. performed MCD

measurements in photodoped ZnO and ITO NCs with the conclusion that the linear field

dependence and temperature independence of MCD signals are signatures of LSPRs in doped

semiconductor NCs, which may have interesting ramifications for low-energy plasmonic

sensing or imaging technologies.[53–55]

The magneto-optical responses measured by MCD spectroscopy provides an opportunity for

study of interface-free plasmon-exciton coupling in single-phase plasmonic metal oxide NCs.

Yin et al.[56] demonstrated an electron polarization in degenerately doped In_2O_3 NCs due to the

non-resonant coupling of cyclotron magneto-plasmonic modes with the excitons at the Fermi

level.[56] Since LSPR and exciton in semiconductor NCs are non-resonant in nature, the proposed mechanism is that the plasmon-exciton coupling is proposed to be mediated by phonons which can transfer angular momentum allowing generation of magneto-plasmonic modes and splitting of the band states. However, more work on the mechanism of plasmon-exciton coupling is necessary to be done both theoretically and experimentally.[56]

1.3.3 Theoretical basis of magnetic circular dichroism

MCD spectroscopy is a useful characterization tool to measure the difference in absorption between left circularly polarized (LCP (ρ^-)) and right circularly polarized (RCP (ρ^+)) beams. For DMSs, the influence of d electrons from magnetic ions on s and p electrons from semiconductors will make conduction band and valence band split depending on spin orientation. The absorption of LCP and RCP will be changed by this spin-polarized semiconductor band structure (Figure 1.11a).[57] For plasmonic semiconductors, the action of external electric and magnetic fields on free carriers in NCs need to be considered. In the presence of an external electric and magnetic field, free electrons in plasmonic NCs experience a Lorentz force, the total force (F) acting on a free electron is:[58]

$$\text{F} = m^* \frac{dv}{dt} + \gamma m^* v = -eE - e(v \times B) \tag{1.7}$$

where m^*, v and e are the effective mass, velocity and charge of the electron, respectively, γ is the damping factor, E is the intensity of external electric field, B is the intensity of external magnetic field.[58]

23

When the circularly polarized light with opposite helicity, left circularly polarized (ρ^-) and right circularly polarized (ρ^+), act on free electrons associated with LSPR, the electric Lorentz force (F_E) induces circular charge motion in opposite directions at the angular frequency equal to that of the incoming light. In the absence of magnetic field, two energetically degenerate plasmonic modes (ω_0) that collectively oscillate are generated. For a magnetic field applied parallel with the light propagation direction, charge traveling with velocity v will experience a magnetic Lorentz force (F_B) that induces motion perpendicular to magnetic field plane and hence in the plane of electric field, causing the shift of circular excitation resonance to either higher or lower frequency (Equation 1.8). The splitting of two cyclotron plasmonic modes leads to a difference in the absorption of LCP (ρ^-) and RCP (ρ^+) beams causing a derivative-shaped spectrum.[56,58,59] The schematic representation is illustrated in Figure 1.11b.

$$\Omega_B^{\pm} = \omega_0 \pm \frac{qB}{2m^*} = \omega_0 \pm \frac{\omega_c}{2} \tag{1.8}$$

Where B is the intensity of the magnetic field, m^* is the effective mass of the mobile charge carrier, and ω_c is the carrier's classical cyclotron frequency.

24
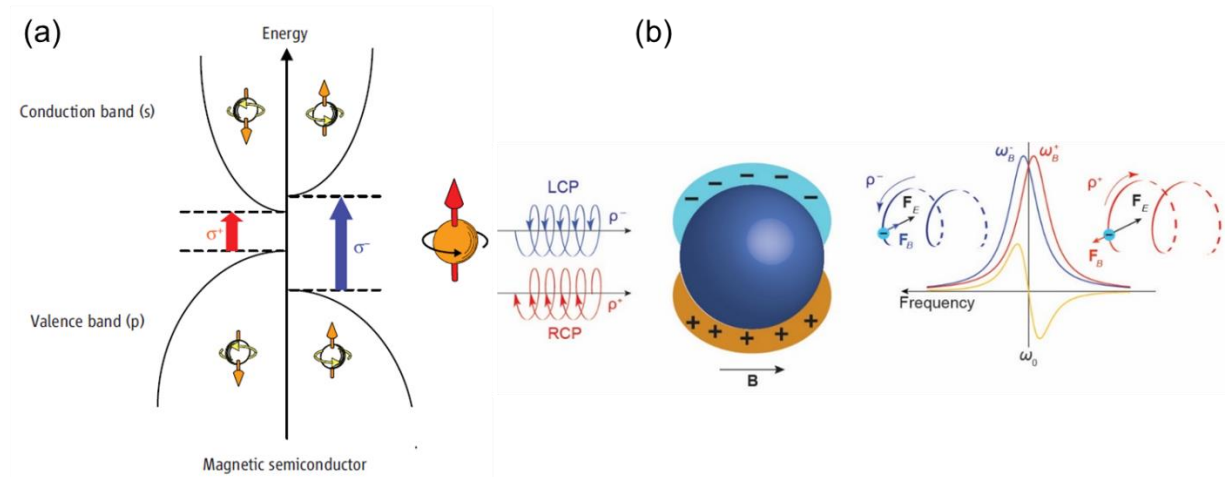
Figure 1.11. (a) Schematic representation of origin of the MCD signal in magnetic semiconductos.[57] (b) Schematic representation of the origin of the MCD signal of LSPR in plasmonic nanocrystals (yellow line), represented as the difference between the absorption of the LCP (ρ^-) beam (blue line) and RCP (ρ^+) beam (red line) for a magnetic field.[56] Reproduced with permission from ref 51. Copyright 2018 Nature.

MCD signal is the sum of three Faraday terms which are A, B, and C terms representing the different contribution from the interaction between ground/excited states and external magnetic field. The basic equation of MCD intensity is expressed as follows:[56,60]

$$\frac{\Delta A}{E} = \gamma \mu_B B \left[A_1 \left(-\frac{\partial f(E)}{\partial E} \right) + \left(B_0 + \frac{C_0}{kT} \right) f(E) \right] \tag{1.9}$$

where ΔA is the differential absorption between the LCP and RCP light, E is the energy ($h\nu$), γ is a constant, and its value is dependent on the chosen unit, μ_B is the Bohr magneton, B is the magnetic field, k is the Boltzmann constant, T is the temperature, A_1, B_0, C_0 are parameters

that describe the A, B, and C terms, respectively, $f(E)$ is the absorption spectrum band shape and $\frac{\partial f(E)}{\partial E}$ is its first derivative.

A term is temperature independent MCD signals with derivative line shape about the degeneracy of excited states (Figure 1.12a). B term is also temperature-independent but shows Gaussian-shaped signal (Figure 1.12b), originating from the mixing effect of the zero-field wavefunctions between nondegenerate states in the presence of magnetic field. Almost all the molecules' MCD signals have B term's contribution, however, B term might be indistinguishable in MCD spectra due to the weaker intensity compared with A or C terms. C term is temperature-dependent due to the ground-state degeneracy under external magnetic field with the shape of Gaussian line.[60,61] C is zero for molecules with nondegenerate ground state, which is for diamagnetic systems, whereas in paramagnetic materials, C term becomes dominant in the MCD spectra especially at low temperature following the Curie-type relationship:

$$M = \frac{N}{T} \tag{1.10}$$

where T is the temperature, and N is the fitting parameter.
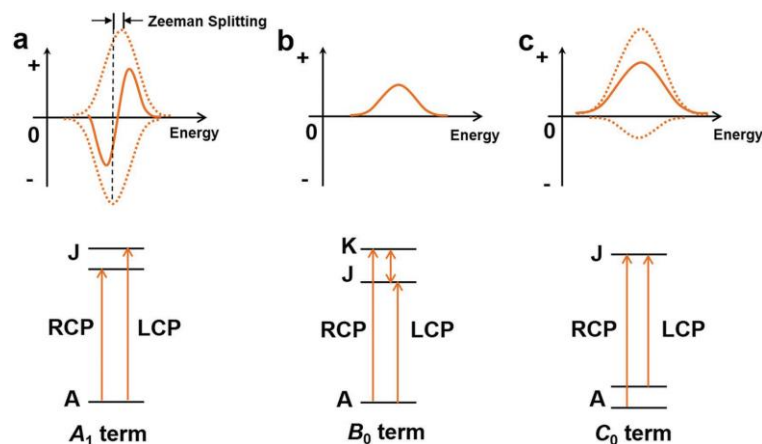
Figure 1.12 The simplified diagram of mechanism of a) A, b) B, and c) C terms in MCD. The dashed curves represent absorption of LCP light (positive peaks along vertical axis) and RCP light (negative peaks along vertical axis). The solid curves in top graphs stand for the resultant MCD responses.[61] Reproduced with permission from ref 56. Copyright 2018 Wiley-VCH.

1.4 Tungsten oxide nanocrystals

Tungsten oxides are one of promising transition metal oxides with various phase transformations and sub-stoichiometric compositions for electrochromic devices, photocatalysis, and sensing capabilities.

Stoichiometric tungsten oxide (WO_3) exhibits a ReO_3-type cubic structure (perovskite-like structure without A-site) with corner sharing of WO_6 octahedra (Figure 1.13). According to the tilting angle and rotation direction of WO_6 octahedra,[62] various phases have been reported including monoclinic II (ε-WO_3), triclinic (δ-WO_3), monoclinic I (γ-WO_3), orthorhombic (β-WO_3), tetragonal (α-WO_3), hexagonal (h-WO_3), and cubic (c-WO_3). Under ambient pressure, the phase transformations of bulk WO_3 can be adjusted through annealing or cooling, following

a clear sequence with temperature: from ε-WO$_3$ ($<$ -43 ℃) to δ-WO$_3$ (-43 to 17 ℃), to γ-WO$_3$ (17-330 ℃), to β-WO$_3$ (330-740 ℃), finally to α-WO$_3$ ($>$ 740 ℃).[63,64] At room temperature, γ-WO$_3$ is the most stable phase with an indirect bandgap of 2.62 eV,[38] where the valence band is mainly composed of O2p orbitals while the conduction band is formed by W5d orbitals.
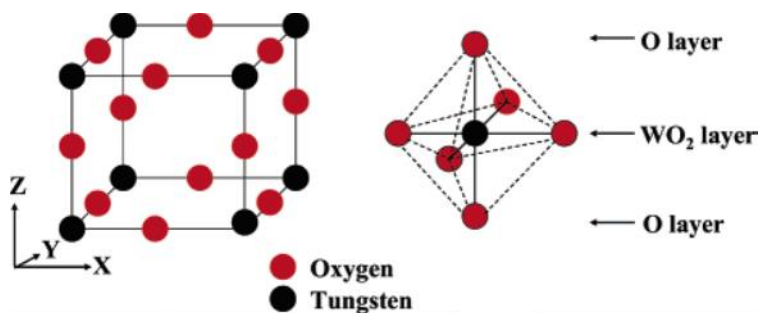
Figure 1.13 The ideal cubic structure of WO$_3$ with WO$_6$ octahedra.[65] Reproduced with permission from ref 60. Copyright 2006 American Chemical Society.

Tungsten oxide is also well-known for sub-stoichiometric compositions because it is able to possess considerable amount of oxygen vacancies by adjusting the synthesis conditions. The oxygen-deficient stoichiometric tungsten oxides (WO$_{3-x}$) generally exhibit a deep blue color, with a variety of compositions including WO$_{2.72}$ (W$_{18}$O$_{49}$), WO$_{2.8}$ (W$_5$O$_{14}$), WO$_{2.83}$ (W$_{24}$O$_{68}$), and WO$_{2.9}$ (W$_{20}$O$_{58}$).[8,66] The elimination of oxygen in WO$_3$ is usually accompanied by structural changes leading to shear planes or pentagonal columns. Particularly, in bulk monoclinic W$_{18}$O$_{49}$, an ordered two-dimensional lattice of edge-sharing WO$_6$ octahedra forming a network of pentagonal columns is interspersed with hexagonal channels.[67] The optical bandgap energy is increased compared to stoichiometric WO$_3$ due to Burstein-Moss

effect. The characteristic LSPR absorption peak in the NIR region can be induced by electrons introduced by oxygen vacancies.[66]

1.5 Zinc oxide nanocrystals

ZnO is a key technological inorganic material with numerous applications in optoelectronic devices, transistors, luminescence materials, catalysts, sensors and transparent electrodes[68,69] because it is an environmentally benign, cost effective material with abundant availability and reduced toxicity. ZnO belongs to the family of II-VI binary compound semiconductors, with a direct bandgap energy ca. 3.37 eV and a large exciton binding energy around 60 meV.[70,71] These characteristics enable ZnO to have photonic applications in the UV or blue spectral range at room temperature.[71] In addition, it can exhibit strong piezoelectric and pyroelectric properties with large electromechanical coupling due to the lack of the center of symmetry.[72] The high optical absorption of ZnO in UVA (315-400 nm) and UVB (280-315 nm) regions is beneficial in antibacterial activity and usage as a UV protector in cosmetics.[73] ZnO is transparent to visible light and can be made highly conductive through the doping process.

ZnO exhibits three different crystal structures namely, rocksalt, zinc-blende and wurtzite, as schematically shown in Figure 1.14. The hexagonal wurtzite structure is the most thermodynamically stable phase at ambient conditions, whose unit cell has two lattice parameters, a and c, in the ratio of c/a=$\sqrt{8/3}$=1.633.[74] The planes composed of tetrahedrally coordinated O^{2-} and Zn^{2+} ions are stacked alternately along the c-axis (as shown in Figure 1.14c). The zinc-blende structure can only be stabilized by growth on cubic substrate, and the rocksalt structure may only be obtained at relatively high pressures.[74]
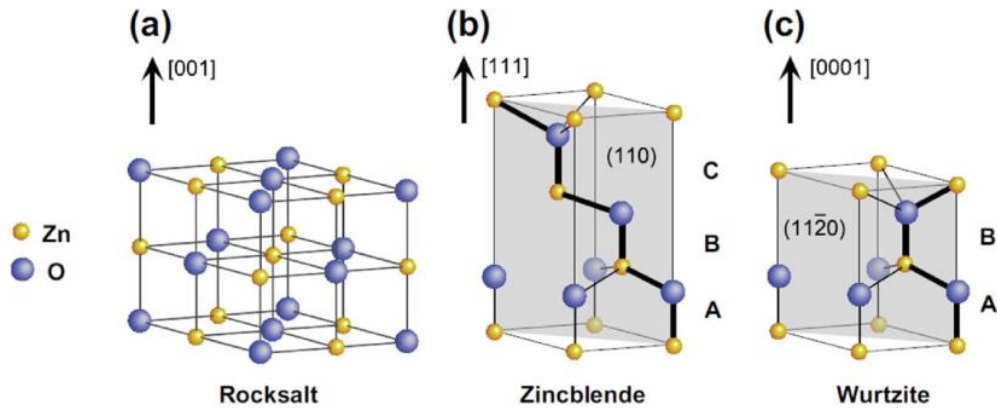
Figure 1.14. Stick and ball representation of ZnO crystal structures: (a) cubic rocksalt, (b) zinc blende and (c) hexagonal wurtzite. The yellow and blue spheres denote Zn and O atoms, respectively.[75] Reproduced with permission from ref 70. Copyright 2018 Elsevier.

Native point defects in ZnO have a strong influence on the electrical and optical properties, a good understanding of their behavior is beneficial for applications.[76] The primitive forms of native point defects in ZnO are oxygen vacancies (V_O), zinc interstitials (Zn_i), oxygen interstitials (O_i) and zinc vacancies (V_{Zn}).[77] Generally, V_O and Zn_i act as donors, while O_i and V_{Zn} act as acceptors.[78] The states of these defects in electronic structures are debatable.[79,80] However, it is certain that ZnO posseses band-edge emission and defect-related visible emission. Oxygen vacancies are the most widely accepted mechanism for the visible emission of ZnO. They have three charge states including singly ionized oxygen vacancies (V_O^+), neutral oxygen vacancies (V_O^X) and doubly ionized oxygen vacancies (V_O^{++}),[81,82] which are singly positively charged, neutral and doubly positively charged relative to the lattice, respectively, the positions of oxygen vacancies in ZnO NWs are illustrated in Figure 1.15. Some calculations of defects in ZnO film has proved that Zn_i is a shallow donor state, energy gap between which

30

and conduction band minimum is ca. 0.5eV.[78] Therefore, the oxygen vacancies (V_O^+ and V_O^X) and zinc interstitials have been suggested to be the source of natural n-type conductivity in ZnO without any dopants.
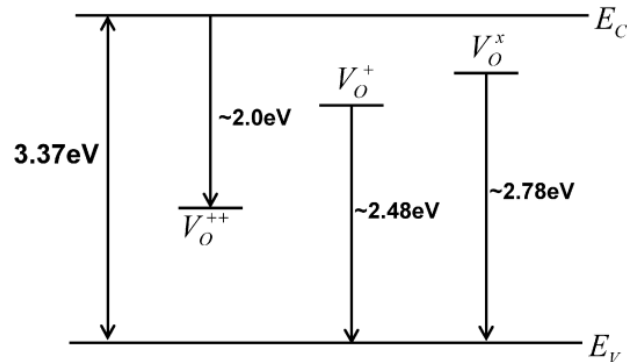
Figure 1.15. Scheme of state of oxygen vacancies and luminescence emission processes in ZnO NWs.[81] Reproduced with permission from ref 76. Copyright 2008 Elsevier.

1.6 Motivation and scope of thesis

The behavior of defects is of great importance in studies of semiconductor NCs as their electrical and optical properties are strongly influenced by defects, leading to various applications including photovoltaics, photocatalysis and magneto-optics.

In the application of photocatalysis, the plasmonic heterostructured photocatalysts with or without noble metals have been extensively studied due to the efficient absorption of solar spectrum from NIR to MIR range and reduction of carrier recombination compared to traditional semiconductor photocatalysts. However, the heterostructured photocatalysts involving noble metals still suffer from the difficulty of industrial production due to the high cost of noble metals, while the heterostructure photocatalysts without noble metals also suffer

from the complexity of design and preparation, which is also a challenge for commercial use. Therefore, the utilization of single-phase plasmonic semiconductor NC photocatalysts is able to overcome these difficulties due to facile synthetic methods and simple configuration as well as the potential to efficiently absorb NIR to MIR portion of solar radiation and consequently enhance photocatalytic activity.

Tungsten oxide is one of the promising transition metal oxides with various phase transformations and it is well known for sub-stoichiometric compositions for photocatalysis. The oxygen vacancies in sub-stoichiometric tungsten oxide can induce the LSPR properties by introducing free electrons leading to the high absorption in the NIR to MIR range, which makes it a great candidate for plasmonic photocatalysts with lower cost than noble metals. In addition, the synthesis method of tungsten oxide is simple compared to heterostructures. More importantly, the sub-stoichiometric tungsten oxides have high optical bandgap energy due to the filling state by electrons introduced by oxygen vacancies, which makes it possible that the conduction band minimum and valence band maximum can straddle the range between the reduction potential of H^+ and the oxidation potential of H_2O.[38] Hence, the sub-stoichiometric tungsten oxide can be an excellent candidate for single-phase plasmonic photocatalysts.

In the application of magneto-optics, previous research has demonstrated exciton-plasmon coupling in single-phase metal oxide nanocrystals such as ITO NCs without interface by using MCD spectroscopy. In the past few decades, a variety of metal oxides with plasmonic properties in the NIR and MIR regions have been reported.[5] Among these metal oxide semiconductors, ZnO is an environmentally benign, cost effective material with abundant

32

availability on earth and reduced toxicity to human and the environment. In order to explore the generality of non-resonant exciton-plasmon coupling in semiconductor NCs, it would be interesting and promising to investigate it in the ZnO system. As mentioned above, ZnO is a natural n-type semiconductor even without any intentional dopants due to native defects providing free charge carriers. It is, therefore, feasible to tune LSPR in ZnO NCs via manipulating defect formation.

Photoluminescence (PL) has been developed as a useful technique to detect point defects in semiconductor NC analysis because it is highly sensitive and non-destructive to the samples.[83] ZnO has strong emission related to defect states, and thus the defect concentration could be detected using PL spectroscopy. It is reported that the annealing atmosphere has an essential effect on the concentration of defects in ZnO nanosheets.[84] Generally, an inert or reducing atmosphere is supposed to create higher concentration of oxygen vacancies due to the deficiency of oxygen supply. On the contrary, an oxidizing atmosphere tends to cause lower concentration of oxygen vacancies because of the rich supply of oxygen.[84] Therefore, in this work, defect concentration was manipulated by tuning synthesis conditions and investigated using PL spectroscopy. These results were then correlated with the results of MCD spectroscopy, allowing for controlling the mechanism of carrier polarization in undoped ZnO NCs.

Although the studies on using plasmonic semiconductor NCs directly in solar energy harvesting and conversion as well as magneto-optical properties are just beginning to emerge, the ability to modify the electronic structure and optical properties of semiconductor NCs via

defect manipulation could provide new opportunities in the field of photocatalysis and information technology.

Chapter 2

Experimental Section

2.1 Materials

All chemical reagents and solvents were used as received from the manufacturers without any further purification. Tungsten hexacarbonyl ($W(CO)_6$) and magnesium acetylacetonate ($Mg(acac)_2$) were purchased from Strem Chemicals, Inc; Zinc stearate ($ZnSt_2$, Zn $[CH_3(CH_2)_{16}COO]_2$, 12.5-14%) was purchased from Alfa Aesar; oleic acid (OA, $CH_3(CH_2)_7CH=CH(CH_2)_7COOH$, 90%), 1-octadecene (ODE, $CH_3(CH_2)_{15}CH=CH_2$, 90%), 1-dodecanol (DDOL, $CH_3(CH_2)_{11}OH$, 98%), Oleylamine ($C_{18}H_{35}NH_2$, 70 %), hexane (98.5%), toluene (99.9%), acetone (99.9%) were purchased from Sigma-Aldrich. Argon (Ar) and nitrogen (N_2) as the high purity carrier gases (grade 5), were obtained from Praxair. The mixture of hydrogen and nitrogen (7% H_2 in N_2) was also obtained from Praxair.

2.2 Synthesis and sample preparation

2.2.1 Synthesis of WO$_{3-x}$ NCs

The synthesis of substoichiometric tungsten oxide NCs was modified on a reported solvothermal method.[85] In a typical reaction, 9 mmol of oleylamine and 27 mmol of oleic acid were mixed in a three-neck round bottom flask. Before heating, the flask will be purged with argon for 10 min and the whole reaction will be under argon atmosphere. when temperature was increased to 100 ℃, 3 mmol of $W(CO)_6$ was added to the flask. After that, the temperature continued to be increased to 300 ℃ and the whole reaction was kept at this temperature for 1

h. Finally, the obtained solution was removed from heating mantle and cooled down to room temperature. A small amount of toluene was added when transferred to test tubes due to the sticky nature of products.

After centrifuging, the precipitate was washed with reagent ethanol three times. A vortex mixer was used to help with agitation of the solution. The precipitate was divided into three equal parts, two parts were dispersed in reagent hexane and toluene for future measurements. The remaining was suspended in reagent acetone, and the resultant slurry was placed on a watch glass to be dried naturally overnight. The final powder products were ground using mortar and pestle and collected in a small vial for photocatalytic reactions.

2.2.2 Synthesis of ZnO NCs

The synthesis of zinc oxide NCs was mainly based on a reported non-injection method.[14] In a typical reaction, 1.89 g (2.99mmol) of $ZnSt_2$ was added to a three neck round bottom flask, then 2.65 g (9.38mmol) of OA, 16.00 g (63.37mmol) of ODE, and 4.80 g (25.76mmol) of DDOL were added to flask successively. At the beginning, the flask was connected to a Schlenk line at room temperature with reasonable stirring. Then the whole setup was degassed for 10 minutes with target gas and subsequently kept under the same gas atmosphere during the entire reaction. The synthesis temperature was firstly increased to 100-140 ℃ and the solution was kept at this temperature range for 30 minutes to ensure all reactants mixed and dissolved evenly. After 30 minutes, the solution was heated to 250 ℃ at a rate of about 4 ℃ per minute and remained at 250 ℃ for 1 h. Finally, the obtained solution was removed from heating mantle and cooled down to room temperature.

After centrifugation of cooled solution, the precipitate was washed with a mixture of toluene and acetone three times. A vortex mixer was used to help with agitation of the solution. The precipitate was divided into three equal parts, two parts were dispersed in reagent hexane and toluene for future measurements. The remaining was suspended in reagent acetone, and the resultant slurry was placed on a watch glass to be dried naturally overnight. The final products were ground using mortar and pestle and collected in a small vial for future measurements.

2.2.3 Synthesis of Mg-doped ZnO NCs

Mg-doped ZnO NCs were synthesized using the same method described for pure ZnO NCs with small changes with adding corresponding amount of $Mg(acac)_2$ based on the certain Mg/Zn ratio and reaction duration being 3 h after reaching 250 ℃.

2.3 Characterization techniques

2.3.1 Powder X-ray diffraction (XRD)

Powder X-ray diffraction (XRD) is a useful characterization tool to identify the structure of crystalline samples. XRD patterns of all samples were collected with an INEL XRD diffractometer with position-sensitive detector and monochromatic Cu-Kα radiation (λ = 1.5418 Å) in Dr. Holger Kleinke's group in the Department of Chemistry at the University of Waterloo. Each sample was ground into a fine powder and collected on a sample holder for a certain time of measurement. XRD patterns can be referenced to a database that consists of known diffraction patterns and processed on Match! software. The particle size can be

estimated from the full width at half maximum of certain diffraction peak using the Scherrer equation:[86]

$$D = \frac{K\lambda}{\beta cos\theta} \tag{2.1}$$

where D is the average particle size (nm), K is numerical constant (0.9), λ is X-ray wavelength (0.15418nm), β is width of the line at the half-maximum intensity and θ is the diffraction angle (radian).

2.3.2 Transmission electron microscopy (TEM)

Transmission electron microscopy (TEM) imaging and energy dispersive X-ray spectroscopy (EDX) provide the information about morphology and elemental composition of NPs. In this work, samples were prepared by depositing a small amount of diluted colloidal NC suspension on copper grids with lacey Formvar/carbon support films purchased from Ted Pella, Inc and measurements were performed on a JOEL-2010F microscope operating at 200 kV at McMaster University. High-resolution TEM (HRTEM) images were analyzed by Gatan Digital Micrograph software.

2.3.3 Ultraviolet-visible-near infrared (UV-vis-NIR) spectrometer

UV-vis-NIR spectroscopy is used to measure the absorption of materials within a certain range of wavelength, where the optical properties (free carrier absorption) and electronic structures (band edge) can be determined. The absorption spectra were collected with Varian Cary 5000 UV-Vis-NIR spectrophotometer at room temperature. The measurements were performed on colloidal suspensions of NPs in hexane for band gap collection in the visible

range from 200 nm to 800 nm or on thin films prepared by drop-casting the colloidal suspensions onto quartz substrates for plasmonic properties test from 200 nm to 3300 nm.

2.3.4 Photoluminescence (PL) spectroscopy

Photoluminescence spectroscopy is used to investigate light emission of samples. All spectra were done at room temperature on a Varian Cary Eclipse fluorescence spectrometer. Samples were prepared by dispersing sample in hexane solvent and put in a cuvette. Pure ZnO NCs were excited at 350 nm with excitation and emission slits set to 10 and 5 nm, respectively. Mg doped ZnO NCs were excited at 325nm with the same excitation and emission slits. 295-1100 nm emission filters were used during data collection.

2.3.5 Fourier transform infrared spectroscopy (FTIR)

FTIR spectroscopy acquires optical properties of samples in the mid-infrared range due to distinct frequencies of vibrations. The organic molecules with different functional groups on the surface of NCs can be identified. FTIR spectroscopy can be applied to measure plasmonic properties as plasmonic semiconductor NCs with large free carrier concentration have broad optical absorption peak in the MIR region. In this study, all FTIR spectra were collected using KBr pellets in the range from 400 to 4000 cm^{-1} on the FTIR Bruker Tensor 37 spectrometer.

2.3.6 Magnetic circular dichroism (MCD) spectroscopy

MCD spectroscopy is used to investigate the different absorption between left (ρ^-) and right (ρ^+) circularly polarized light ($\Delta A = A_L - A_R$) in the presence of an external magnetic field which is parallel to the direction of light propagation (set-up shown inFigure 2.1). The

MCD intensity is measured as the degree of ellipticity (θ) in millidegrees of transmitted light, which can be converted to $\frac{\Delta A}{A}$ to compare the intensity of MCD band for different samples using the following relationship:

$$\frac{\Delta A}{A} = \frac{\theta}{32982 \times A} \qquad (2.2)$$
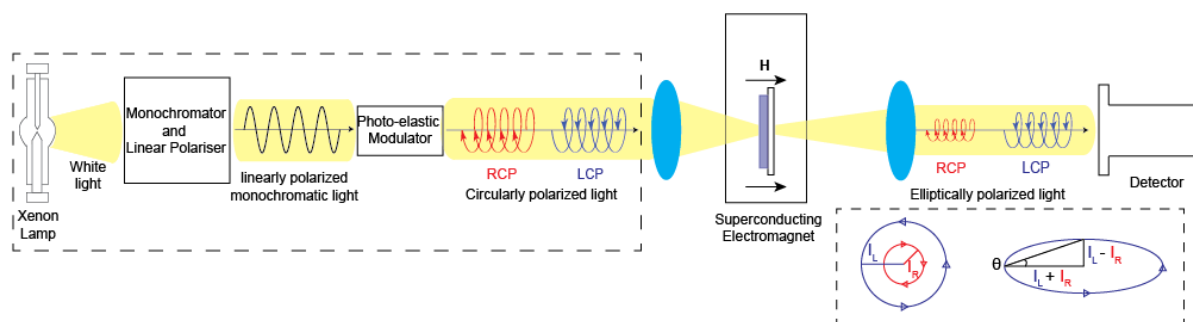
Figure 2.1 The set-up of MCD spectrometer. A light from Xenon lamp is passed through a monochromator and polarizer to generate a linearly polarized monochromatic light. Then it is passed through a photoelastic modulator to create left and right circularly polarized light. A sample is mounted in a superconducting magneto-optical cryostat with magnetic field parallel to the light propagation direction. LCP and RCP light are absorbed to a different degree when passing through the sample. The differences of left and right circularly polarized light (I_L and I_R, respectively) are combined to form an elliptically polarized beam. The degree of ellipticity, θ, is defined as the angle between the long and short axes of the ellipse.

MCD spectra were collected in Faraday configuration by a Jasco J-815 spectropolarimeter for generating circularly polarized light and signal detection. Samples were prepared by depositing colloidal NP suspension on strain-free quartz substrates and subsequently placed in

an Oxford SM 4000 magneto-optical cryostat allowing for variable temperature (5 to 300 K) and variable field (0 to 7 T) operation.

The excitonic magnetic field-dependence intensities of MCD spectra were collected at variable fields from 1 T to 7 T, all spectra need to be subtracted by baseline spectrum collected at 0 T before data analysis. The subtracted field-dependent integrated intensities were fitted to spin-only Brillouin function:

$$M_S = \frac{1}{2} N g_S \mu_B \left[(2S+1) \coth \left((2S+1) \frac{g_S \mu_B B}{2 k_B T} \right) - \coth \left(\frac{g_S \mu_B B}{2 k_B T} \right) \right] \qquad (2.3)$$

where S is the spin quantum number, g_S is the corresponding Landé g-factor, B is the external magnetic field, k_B is the Boltzmann constant and T is the temperature. $g_S = 2.002$ and $S = 1/2$ were used for the fitting in the scenario of free electrons and N was the fitting parameter.

2.4 Photocatalysis

2.4.1 Photocatalytic activity evaluation

A 100 mL jacketed temperature-control beaker was connected to Cole-Parmer Polystat 6-liter Refrigerated Circulating Bath with certain fixed temperature. Then 50 mL of dye solution (5mg/L) was added into the beaker by using a 25 mL volumetric pipette twice. A thermometer was put in the beaker to monitor the solution temperature. After the target temperature was reached, 12 mg of catalyst was added into the beaker with reasonable stirring. The beaker was put in a small dark room wrapped with foil to protect it from ambient light and stirred on a stir plate where a vortex was formed in solution. The flask was situated ~20 cm under two 40 W

41

254 nm lamp and a 250W incandescent red bulb in the case of UV and IR measurements, respectively.

The initial measurement of this solution was taken on the UV-Vis spectrophotometer before adding the photocatalysts. After that, an aliquot of solution was taken in a cuvette for absorption test and then returned to the reaction vessel to keep the volume of the dye constant in the beaker. This was performed every 20 min intervals to observe the change in absorbance.

2.4.2 Annealing

The collected powder products were annealed at varying temperature remove the organic ligands and change the defects density. A small amount of WO_{3-x} powder was put in a crucible which was then placed in a pre-heated furnace at the appropriate temperature (200 ℃, 400 ℃, 600 ℃ and 800 ℃) and annealed for 2 hours.

2.4.3 Recyclability

To test the recyclability, after photocatalytic reactions were done, the particles were allowed to settle to the bottom of the flask, taking approximately 2 hours. Then a 2.5 mL aliquot was removed from the flask and 2.5 mL of 100 mg/L Rh-590 dye was added to the flask to make 5 mg/L solution. Then photocatalysis was followed as previously outlined.

2.4.4 Scavenger

Scavenger experiments were done by immediate addition of a scavenger ($FeCl_3$, ascorbic acid, isopropanol, methanol) after adding photocatalysts to achieve a concentration of 10 mM. The reaction and measurements were then carried out as described.

Chapter 3

Plasmonic Photocatalysis of WO_{3-x} NCs

3.1 Structural characterization of WO_{3-x} NCs

X-ray diffraction pattern was collected to identify the crystal structure of WO_{3-x} NC samples (Figure 3.1a) with the diffraction peaks corresponding to the monoclinic $W_{18}O_{49}$ phase (JCPDS No.00-005-0392). Different batches using the same synthesis method have been made to confirm the repeatability of produced samples possessing the same crystal structure (Figure 3.1b). The two relatively sharp peaks are attributed to (010) and (020) crystallographic orientations suggesting the NCs grow along the [010] direction. This result is also in good agreement with high-resolution transmission electron microscopy (HRTEM) image (Figure 3.2c). The lattice spacing is 3.81 Å, close to the reference lattice spacing of 3.78 Å for (010) plane. Figure 3.2a, b illustrates low-magnification and high-magnification transmission electron microscopy (TEM) images of the WO_{3-x} NCs exhibiting the nanorod morphology. They are highly crystalline and uniformly distributed with the average length around 45 nm and diameter around 6 nm.
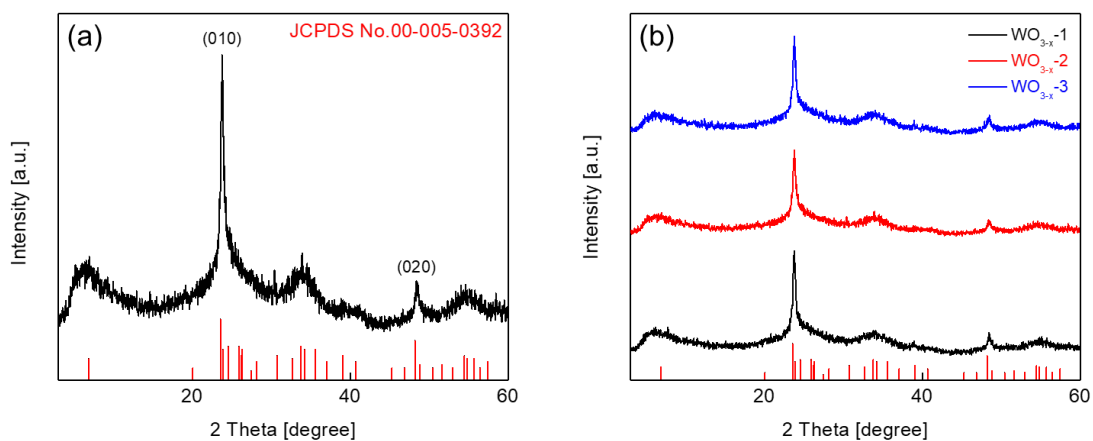
Figure 3.1 XRD patterns of (a) WO_{3-x} NCs; (b) WO_{3-x} NCs from different batches using the same synthesis method. The red vertical lines correspond to the reference XRD pattern of monoclinic $W_{18}O_{49}$ (JCPDS No.00-005-0392).
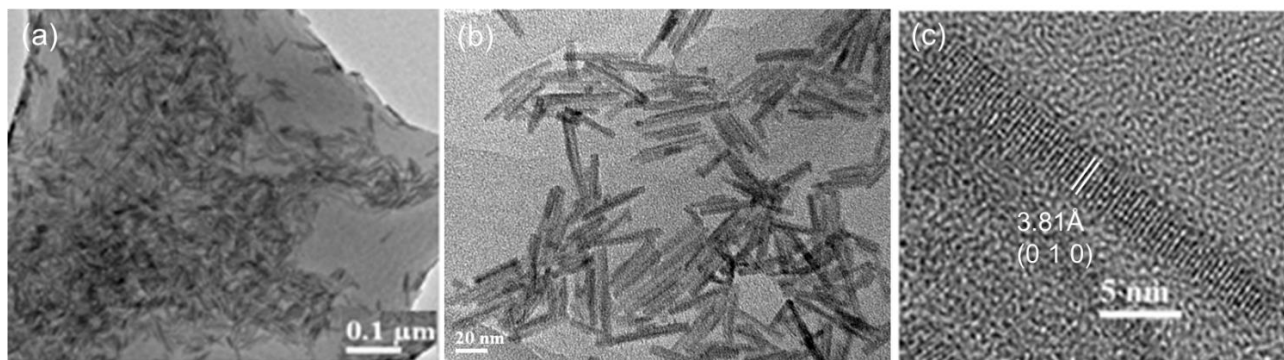
Figure 3.2 (a) Low-magnification TEM image and (b) High-magnification TEM image of WO_{3-x} nanorods. (c) HRTEM image of WO_{3-x} nanorods.

3.2 Optical properties of WO_{3-x} NCs

UV-Vis absorption measurements were performed to monitor the absorption and calculate the approximate optical band gap using Tauc plot according to the equation:

$$(\alpha h v)^n = A(h v - E_g) \tag{3.1}$$

where α is absorption coefficient, h is Planck's constant, v is the frequency of light, A is a material related constant, E_g is bandgap energy, and n equals to 1/2 for an indirect semiconductor or 2 for a direct semiconductor.

Since WO_3 is an indirect semiconductor, $(\alpha h v)^{1/2}$ is plotted versus $h v$ from which the optical bandgap energy is obtained by extrapolating the straight-line portion-of the absorbance increase.[87] The TEM images reveal that the samples are much larger than the exitonic Bohr radius, $a_B = 3$ nm,[88] hence, the bandgap energy is not affected by quantum confinement (QC) effect. In Figure 3.3a, the obtained optical band gap energy of as-synthesized WO_{3-x} nanorods is 3.26 eV which is largely blue-shifted compared to the bulk WO_3 ($E_g = 2.62$ eV), [63] which is attributed to the filling of the conduction band from electrons introduced by oxygen vacancies (Burstein-Moss effect). Figure 3.3b shows the NIR absorption of WO_{3-x} nanorods. A broad light absorption across the visible region approximately starting from 500 nm to NIR region is observed indicating the characteristic LSPR peak is formed by large free carrier concentration in the oxygen-deficient WO_{3-x} nanorods.
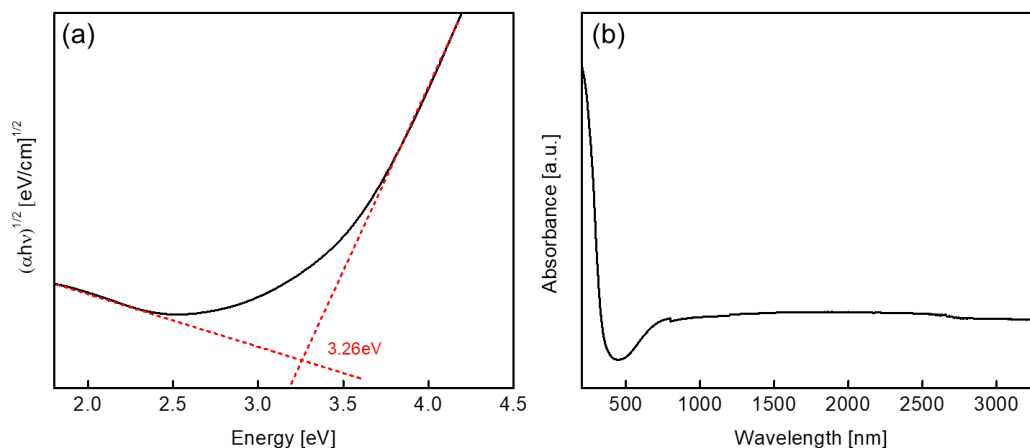
Figure 3.3 (a) Tauc plot of the optical bandgap for WO_{3-x} nanorods. (b) NIR absorption spectra of WO_{3-x} nanorods.

3.3 Photocatalysis

In order to investigate plasmonic photocatalysis, the photocatalytic activity of WO_{3-x} NC samples was evaluated by monitoring the degradation of Rh-590 dye over time in the dark without any light irradiation. According to Beer-Lambert law, the relative change in concentration of Rh-590 (C/C_0) is equal to the relative change in absorbance (A/A_0), where A_0 is the initial absorbance corresponding to the initial concentration (C_0). A_0 was determined by the dye solution before adding photocatalysts instead of after reaching absorption-desorption equilibrium, because the photocatalytic reaction and adsorption-desorption process proceed simultaneously in the case of plasmonic photocatalysis. Previous experimental results show semiconductor photocatalytic oxidation of various dyes fitted the Langmuir-Hinshelwood (L-H) kinetics model:[89]

$$r = -\frac{dC}{dt} = \frac{kKC}{1+KC} \qquad (3.2)$$

where r is oxidation rate of the reactant (mg/L min), C is the concentration of the reactant (mg/L), t is illumination time (min), k is the reaction rate constant (mg/L min) and K is the adsorption coefficient of the reactant (L/mg).

When the starting concentration of the reactant is extremely small, the equation can be simplified to first order reaction:[89,90]

$$ln\frac{C_0}{C} = kKt = k_{app}t \qquad (3.3)$$

where k_{app} is the apparent rate constant (min^{-1}). Plotting $ln\frac{C_0}{C}$ versus time represents a linear plot, the slope of which equals to the apparent first-order rate constant k_{app}.

As shown in Figure 3.4a, WO$_{3-x}$ NCs show excellent performance with almost complete degradation of Rh-590 within 120 min in the dark at 20 ℃, lower than room temperature. Figure 3.4b shows the Langmuir-Hinshelwood plot with excellent linear fit (R^2=0.99492) indicating the apparent rate constant k_{app} to be 0.03285 min^{-1}.
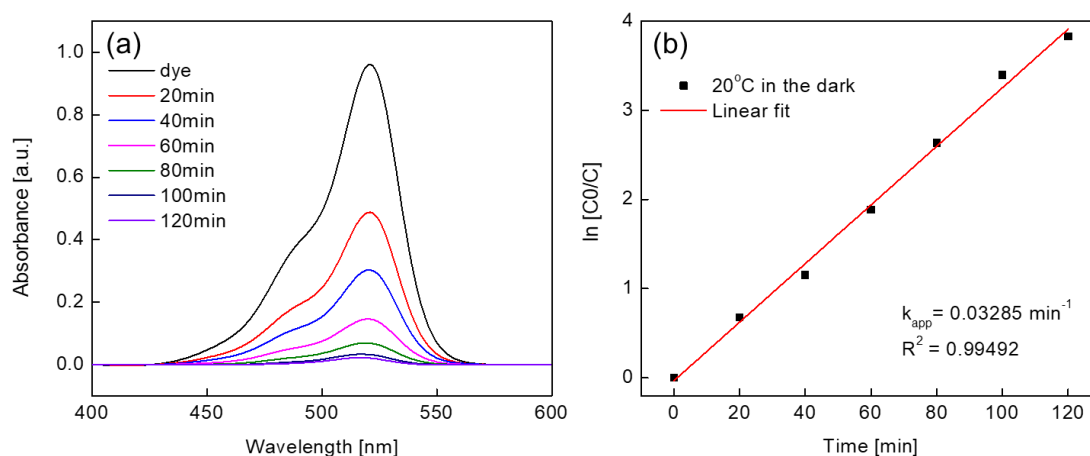
Figure 3.4 (a) Absorption spectra of Rh-590 monitored over time in the presence of WO_{3-x} photocatalysts in the dark at 20 ℃. (b) Langmuir-Hinshelwood plot for Rh-590 photocatalytic degradation in the presence of WO_{3-x} photocatalysts in the dark at 20 ℃. Straight line is the linear fit to the experimental data using Equation 3.3.

3.3.1 Photocatalysis evaluation with control experiments

The photocatalytic reactions were carried out in the presence of different catalysts including as-synthesized WO_{3-x} samples and commercial bulk powders of $WO_{2.9}$ and WO_3 in the dark at 20 ℃. Both as-synthesized WO_{3-x} samples and $WO_{2.9}$ powders are non-stoichiometric exhibiting a deep blue color, while the stoichiometric WO_3 powders are green. Figure 3.5 shows the relative change in concentration of Rh-590 over time in the absence and presence of catalysts. The absorption measurement in the absence of catalysts was conducted to confirm the dye is not self-degraded under identical conditions. From Figure 3.5, there is clearly no

self-degradation, instead, there is a small increase in the absorbance of dye due to the evaporation of solvent during the reaction.

Regarding the reactions in the presence of photocatalysts, as-synthesized WO_{3-x} samples degrades almost completely after 2 hours compared to the commercial powders with $WO_{2.9}$ having a better performance than WO_3. For the reaction in the presence of WO_3 powders, there is a small drop in the first 20 minutes because the adsorption-desorption equilibrium has been reached, but after that, there is no activity at all. $WO_{2.9}$ powders are catalytically active to some degree, but the reaction rate is still much slower than WO_{3-x} samples. The activity trend is in agreement with the trend of the concentration of oxygen vacancies responsible for the generation of free electrons. As-synthesized WO_{3-x} samples have highest concentration of oxygen vacancies, WO_3 samples have the lowest concentration and $WO_{2.9}$ is in the middle. Therefore, the oxygen vacancies contributing to LSPR play an active role in the photodegradation process.
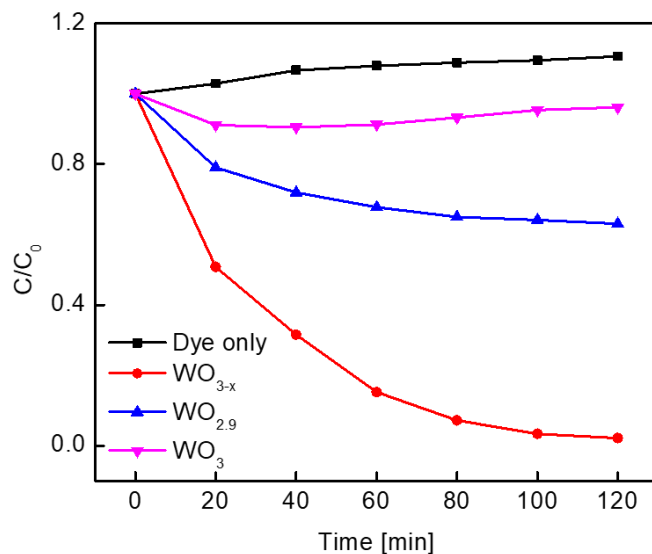
Figure 3.5 The relative change in concentration of Rh-590 (C/C_0) over time in the absence of catalysts as well as in the presence of WO_{3-x}, $WO_{2.9}$ and WO_3 photocatalysts at 20 ℃ in the dark.

Another set of control experiments were conducted by preparing the photocatalysts via annealing of as-synthesized WO_{3-x} NCs at different temperatures, namely 200 ℃, 400 ℃, 600 ℃ and 800 ℃. Figure 3.6a shows the XRD patterns of as-synthesized and annealed WO_{3-x} NCs. A phase transfer from monoclinic $W_{18}O_{49}$ to monoclinic WO_3 can be observed starting at 400 ℃. Apart from the phase changes, diffraction peaks become stronger and sharper with increasing annealing temperature. These two changes indicate the oxygen vacancies are saturated and larger domains are formed in WO_{3-x} after annealing process. Figure 3.6b plots the degradation of Rh-590 in the presence of annealed samples compared to as-synthesized samples. For samples annealed at 200 ℃, they are still photocatalytically active, but the

50

performance reduces significantly because some of the oxygen vacancies are saturated while crystal phase is unchanged. For samples annealed at other temperatures, they have decreased adsorption in the first 20 min as temperature increases due to the relatively small surface-to-volume ratio of large NCs at high annealing temperature (see XRD patterns). After the first 20 min, they all show no activity within 100 min because of the saturation of oxygen vacancies. These control experiments using annealed WO_{3-x} NCs corroborate the essential role of oxygen vacancies and/or free electrons introduced by oxygen vacancies in photodegradation of Rh-590 by tungsten oxide catalysts in nanostructured form.
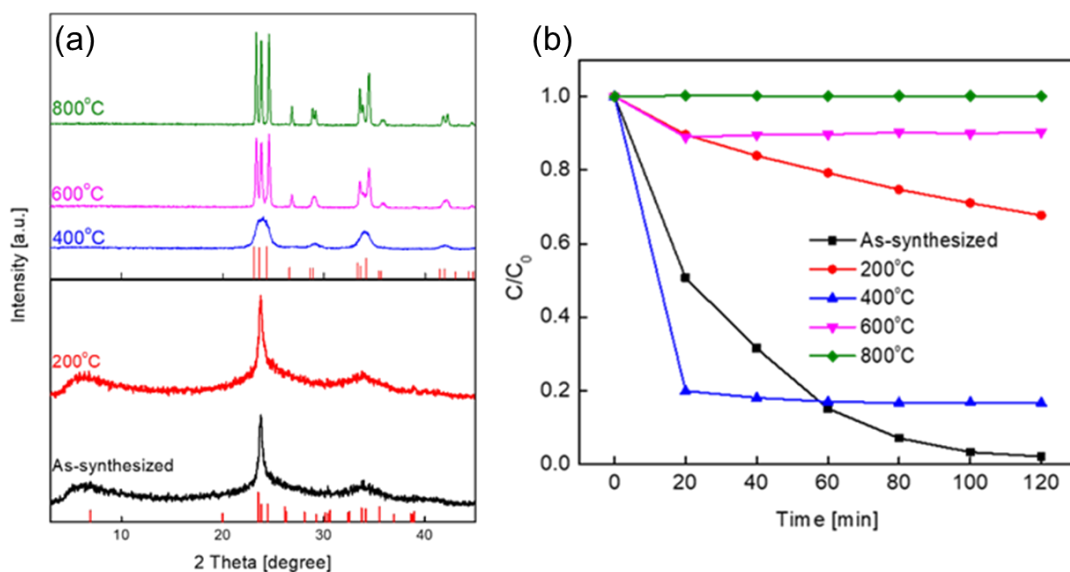
Figure 3.6 (a) XRD patterns of as-synthesized WO_{3-x} NCs and WO_{3-x} NCs annealed at different temperatures. (b) The relative change in concentration of Rh-590 (C/C_0) over time in the presence of as-synthesized WO_{3-x} NCs and WO_{3-x} NCs annealed at different temperatures in the dark at 20 °C.

51

3.3.2 Temperature effect

The temperature effect of photocatalytic reactions was determined at different temperatures in the dark and each kinetic measurement was performed at least three times to determine the standard deviation. Figure 3.7a and b demonstrates the degradation of Rh-590 and the Langmuir-Hinshelwood plots (together with the corresponding linear fits ($R^2 \geq 0.99$)) of the kinetic data for WO_{3-x} NCs at different temperatures, respectively. The obtained apparent rate constants with respect to different reaction temperatures are shown in Figure 3.7c. The photocatalytic degradation rate can generally increase to some degree with increasing reaction temperature due to the modification of the kinetic and activation energy,[91] as well as the increased oxidation rate of dye at the interface.[92] For plasmonic NCs particularly, besides these general reasons, the heat also acts as the IR irradiation source which can excite the LSPR in WO_{3-x} based on blackbody irradiation stating that all objects with a temperature above absolute zero (0 K) emit energy in the form of electromagnetic radiation. According to Wien's Displacement Law, the wavelength at the emission peak λ_{max}, is inversely related to absolute temperature T:[93]

$$\lambda_{max}T = \text{constant} \tag{3.4}$$

The constant is generally given as 2898 μm K.[93]

The calculated wavelength maximum of radiation at different temperatures using Equation 3.4 is shown in Table 1, λ_{max} decreases as the temperature increases. Although the LSPR band for sub-stoichiometric WO_{3-x} nanorods is very broad, the reported band maximum of the plasmon lies in the NIR-MIR range.[5,8] An assumption is that the closer irradiation peak is to

LSPR peak maximum, the more free electrons will participate in the catalytic reaction. In other words, the reaction at 40 ℃ with the smallest radiation wavelength can excite most "hot electrons" for degradation of dyes among all temperatures.
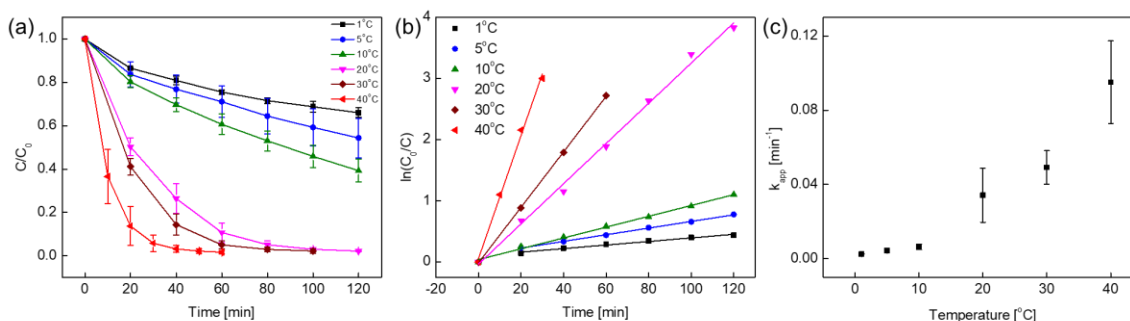
Figure 3.7 (a) The relative change in concentration of Rh-590 (C/C_0) over time in the presence of WO_{3-x} photocatalysts in the dark at different temperatures. (b) Langmuir-Hinshelwood plots of the Rh-590 photocatalytic degradation for WO_{3-x} NCs at different temperatures. (c) Temperature dependence of the apparent rate constant of Rh-590 degradation.

Table 1 The calculated wavelength maximum of blackbody radiation based on Wien's Displacement Law.

Temperature (℃)	1	5	10	20	30	40
λ_{max} (μm)	10.571	10.419	10.235	9.886	9.560	9.254

To further explore the role of oxygen vacancies and LSPR in the photocatalytic reactions were performed under UV at different temperatures including 1 ℃, 5 ℃ and 20 ℃. In Figure 3.8a, the reactions under UV light always exhibit a better performance than the reactions in the

53

dark at each corresponding temperature because the performance under UV actually is the combination of two catalytic effects originating from UV-excited electrons and defect-induced electrons. Therefore, the degradation of Rh-590 solely from UV-excited electrons is the difference between the degradation under UV light and in the dark. As seen in Figure 3.8b, the differences for degradation at each temperature follow the increasing trend as temperature increases (the first 40 min of reaction at 20 ℃ because after that the degradation is almost completed), but the extent of degradation is much smaller than that in the dark. This suggests that the temperature-dependent modification of kinetic energy and activation contributes in a relatively minor way. Such effects could be associated with the presence of a high density of oxygen vacancies on NC surfaces. On the other hand, the defect-induced electrons appear to make a more significant contribution to the degradation of Rh-590 in the presence of WO_{3-x} NCs.
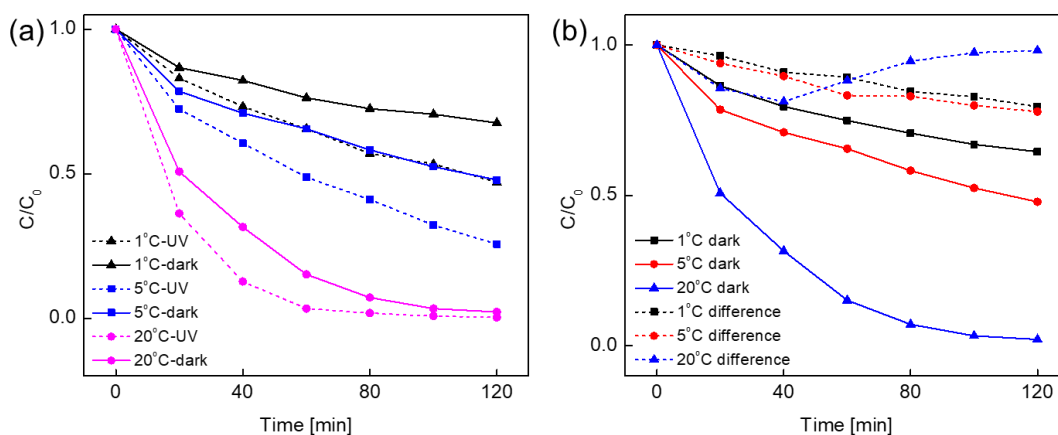
Figure 3.8 (a) The degradation of Rh-590 over time in the presence of WO_{3-x} NCs both under UV light and in the dark at 1 ℃, 5 ℃ and 20 ℃. (b) The comparison between the degradation

of Rh-590 over time in the presence of WO_{3-x} NCs both in the dark and degradation differences between reactions under UV light and in the dark.

The previously mentioned control experiments using bulk WO_3, $WO_{2.9}$ powders and annealed WO_{3-x} NCs as photocatalysts were also conducted under UV light at the same temperature (20 ℃). The non-active catalysts in the dark, bulk WO_3 powders and 800 ℃-annealed WO_{3-x} NCs, show catalytic activity under UV light due to the UV-promoted free electrons, although with a relatively small reaction rate. WO_{3-x} NCs show the best performance both in the dark and under UV light, which we believe is due to defect-induced free electrons.
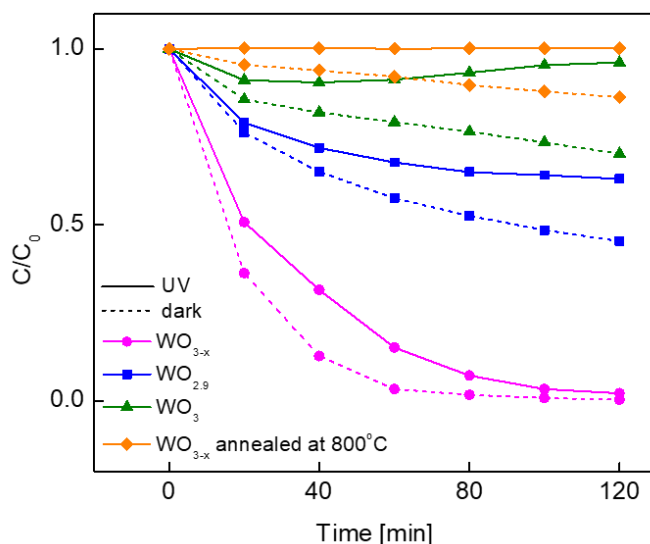
Figure 3.9 The degradation of Rh-590 over time in the presence of WO_{3-x} NCs, bulk WO_3 and $WO_{2.9}$ powders, and 800 ℃-annealed WO_{3-x} NCs photocatalysts both under UV light and in the dark at 20 ℃.

3.3.3 Photocatalysis under IR irradiation

The photocatalytic reactions were performed directly under incandescent IR lamp at the lowest temperature (1℃) to minimize the temperature effect. A control experiment has been conducted to confirm the dye is not self-degraded under IR irradiation. From Figure 3.10, no self-degradation has been observed. When compared with the catalytic reactions in the dark, the performance of WO_{3-x} NCs under IR light is much better than the performance in the dark at 1 ℃ and similar to the that in the dark at 5 ℃. It should be noted that the temperature of dye solution increases to 6 ℃ after 120 min due to the heating effect of IR lamp. Given the heating would be a gradual process, although it is difficult to identify the exact time it takes to increase the temperature to 6 ℃, this result indicates the IR lamp with natural heating effect plays a better or similar role in the catalytic reaction compared to the role of temperature as the irradiation source and further indicates these WO_{3-x} NCs are IR-active catalysts.
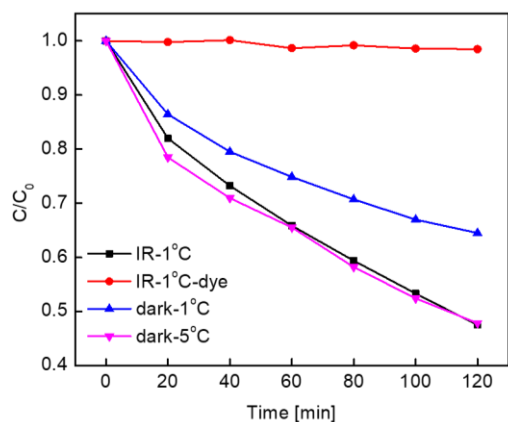
Figure 3.10 The degradation of Rh-590 over time in the presence and absence of WO_{3-x} NCs under IR light at 1 ℃ and the degradation of Rh-590 over time in the presence of WO_{3-x} NCs at 1 and 5 ℃ for comparison.

3.3.4 Recycling

To assess the recyclability of WO$_{3-x}$ NCs, the photodegradation reaction of Rh-590 was conducted in 3 consecutive cycles under identical conditions (at 20 ℃ or 30 ℃ in the dark). As indicated in Figure 3.11a, WO$_{3-x}$ NCs possess high photocatalytic activity after 2 cycles but with a notable drop to 68.9% in the third run. The drop is associated with the strong adsorption of a fraction of dye molecules which block a portion of the surface sites.[94] This strong adsorption could also be a consequence of oxygen vacancies on NC surfaces, which would render tungsten surface sites under-coordinated. However, at a high temperature, more free radicals are present fostering fast cracking reactions, and leading to a high recyclability at 30 ℃ with 82.6% degradation percentage over 3 cycles.
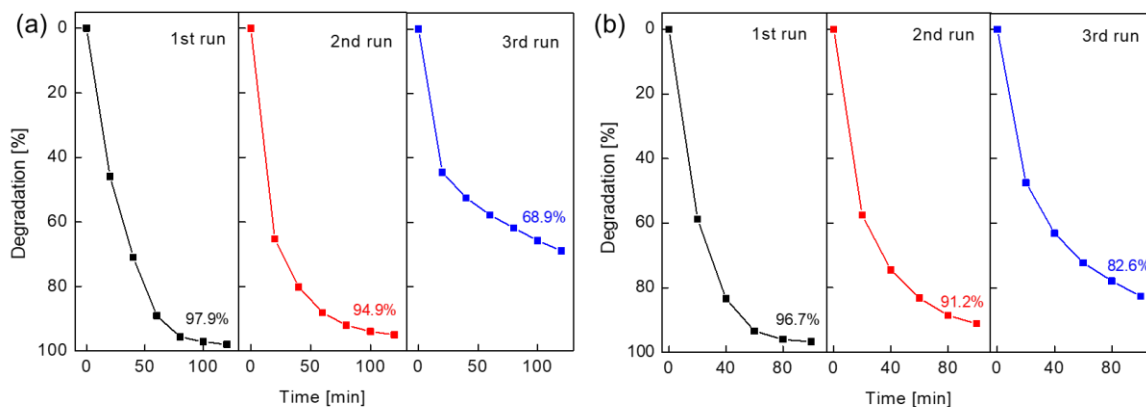
Figure 3.11 Percentage of degradation of Rh-590 using WO$_{3-x}$ NCs over 3 cycles (a) at 20 ℃ (b) 30 ℃.

3.3.5 Scavengers

Various scavengers were employed to probe the role of different redox species in the photocatalytic degradation of Rh-590 in the presence of WO_{3-x} NCs. Figure 3.12 shows the relative decrease in the percentage of degradation upon the addition of selected scavengers. As a result, all tested scavengers decrease the activity of the catalyst, so electrons, holes, hydroxyl radicals and superoxide radicals all take an active role in photocatalytic degradation of Rh-590. Particularly, in the presence of $FeCl_3$ (electron scavenger) and ascorbic acid ($O_2^{\cdot-}$ radical scavenger), the degree of degradation percentage is strongly decreased, indicating the significant role of electrons and $O_2^{\cdot-}$ radicals. $O_2^{\cdot-}$ radicals are also related to electrons because they are formed by adsorbed oxygen and electrons.[95] As I mentioned above, the ability to strongly adsorb oxygen, owing to the presence of oxygen vacancies on NC surfaces, could enable efficient formation of $O_2^{\cdot-}$ radicals. Therefore, the role of conduction band electrons may primarily be the generation of $O_2^{\cdot-}$ radicals as oxidizing agents. Regarding the other two scavengers, methanol (MeOH) and isopropanol (i-PrOH) are known as efficient hole scavenger and $OH\cdot$ radical scavenger, respectively. The photocatalytic oxidation is both inhibited in the presence of these two scavengers, but the stronger reduction in the degree of dye degradation by addition of i-PrOH compared to methanol indicates the formation of $OH\cdot$ radicals come from both electrons and holes.[95] Therefore, reactive radicals including $OH\cdot$ and $O_2^{\cdot-}$ radicals play an important role in dye degradation, and the main effect of free charge carriers is to form these radicals. As an n-type sub-stoichiometric material, WO_{3-x} NCs possess larger concentration of free electrons than holes, which is the reason why there is more significant

inhibition of degradation percentage of Rh-590 in the presence of FeCl$_3$ than in the presence of methanol.
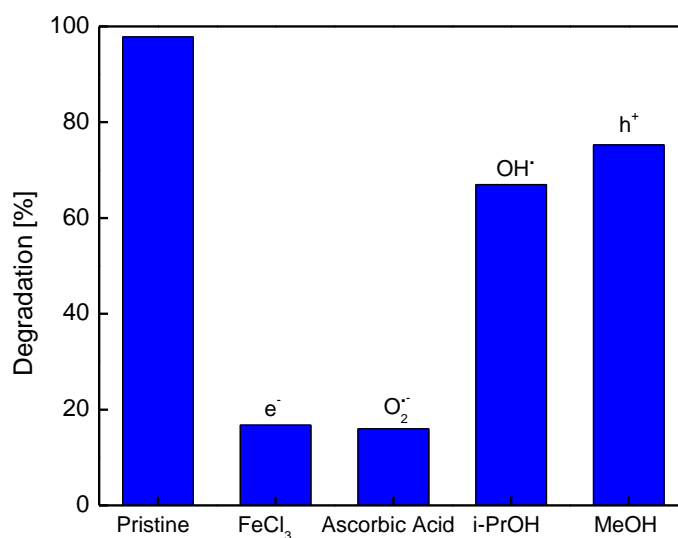
Figure 3.12 Percentage of the photocatalytic degradation of Rh-590 using WO$_{3-x}$ NCs in the dark at 20 °C, in the presence of various scavengers, as indicated in the graph.

3.4 Conclusions

In summary, colloidal WO$_{3-x}$ NCs were successfully synthesized with monoclinic W$_{18}$O$_{49}$ phase in the shape of nanorods. Absorption spectra of WO$_{3-x}$ NCs indicates the large optical band gap and broad absorption in the visible-to-NIR range associated with large concentration of free electrons introduced by oxygen vacancies due to the sub-stoichiometric nature. WO$_{3-x}$ NCs exhibit a superior photocatalytic activity compared to bulk stoichiometric WO$_3$ and sub-stoichiometric WO$_{2.9}$ powders with approximately complete Rh-590 degradation (97.8%)

within 2 hours in the dark at 20 ℃. A series of nanostructured tungsten oxide photocatalyst samples were prepared by annealing as-synthesized WO_{3-x} NCs at various temperatures from 200 ℃ and 800 ℃ accompanied by the phase transformation from monoclinic $W_{18}O_{49}$ to monoclinic WO_3. This result is consistent with annealed samples (starting from 400 ℃) having no photocatalytic activity due to the saturation of oxygen vacancies. More importantly, photocatalytic performance of WO_{3-x} NCs has been improved with increasing temperature. The degradation percentage of Rh-590 in the presence of WO_{3-x} NCs at 30 ℃ can retain 82.6% after 3 cycles showing a good recyclability. Using appropriate scavengers, it was inferred that reactive radicals (O_2^{-} and OH·) play an important role in the mechanism of photocatalytic degradation by WO_{3-x}. While the mechanism of the catalytic activity of WO_{3-x} nanorods requires further investigation, we hypothesize that oxygen vacancies play a key role in their unique behavior for two main reasons: i) they enable an effective adsorption of reactive species on NC surfaces, and ii) lead to the generation of plasmonic properties that could be photo-thermally excited. The results of this work demonstrate the important role of LSPR-associated free electrons originating from oxygen vacancies in single-phase plasmonic semiconductor NCs for photochemical reactions.

Chapter 4

Study of Magneto-optical Properties in ZnO NCs

4.1 Pure ZnO NCs

4.1.1 Crystal structure and morphology of ZnO NCs

ZnO NCs were synthesized under different atmosphere including air, argon, nitrogen and 7% hydrogen in nitrogen (referred to hydrogen in the following text) to manipulate the defect density, whose crystal structures were confirmed by XRD patterns. As illustrated in Figure 4.1, the XRD patterns of all samples correspond to the reference patterns of bulk wurtzite structure of ZnO without detection of any secondary phases. The peaks for air-synthesized ZnO NCs are sharper and stronger than the peaks of other samples, indicating the larger sizes of air-synthesized ZnO NCs based on Scherrer equation.

The size difference between ZnO NCs synthesized under air and hydrogen can also be observed in the TEM images. For ZnO NCs prepared under hydrogen atmosphere, the low-resolution TEM image (Figure 4.2a) shows the NCs have spherical or quasi-spherical shapes with uniform size distribution. Additionally, the ZnO NCs are highly crystalline as illustrated in high-resolution TEM images (Figure 4.2c, d) with two lattice spacings around 2.5 Å and 2.8 Å, which are attributed to (101) and (100) plane of bulk wurtzite ZnO, respectively. For ZnO NCs prepared under air, they exhibit irregular shapes with relatively uniform size distribution (Figure 4.3a). High-resolution TEM images of individual NCs show the lattice spacing is around 2.8 Å which corresponds to the (100) plane of bulk wurtzite ZnO. According to the size

distributions in Figure 4.2b and Figure 4.3b, the average size is 9.3 ± 0.7 nm for ZnO NCs synthesized under air and 21.0 ± 3.5 nm for ZnO NCs synthesized under hydrogen, which is in good agreement with XRD results. The air-synthesized ZnO NCs tend to have larger sizes because the oxidizing condition (air atmosphere) can saturate the oxygen vacancies and the water molecules in the air may provide hydroxyl groups accelerating NC growth during ZnO NC synthesis process.
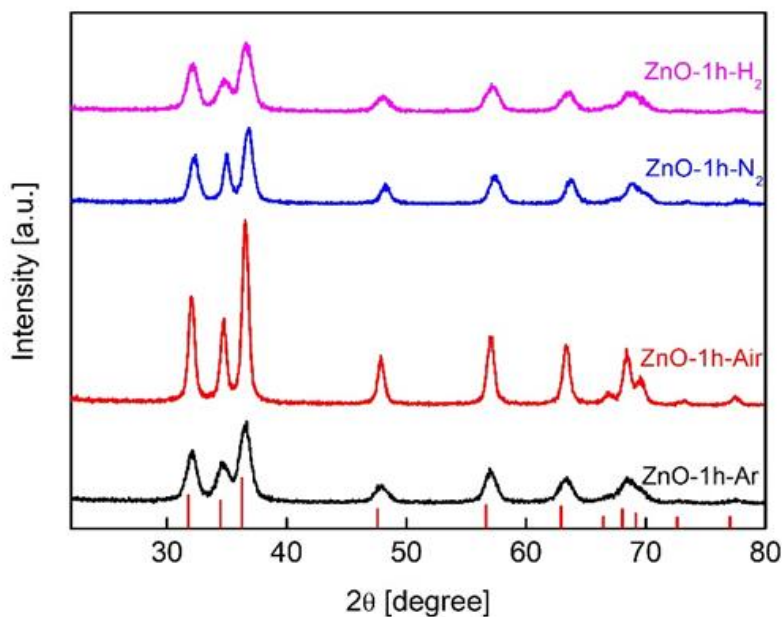
Figure 4.1 XRD patterns of ZnO NCs synthesized under Ar, air, N_2 and 7% H_2 in N_2, as indicated in the graph. The red vertical lines correspond to the reference pattern of bulk wurtzite ZnO.
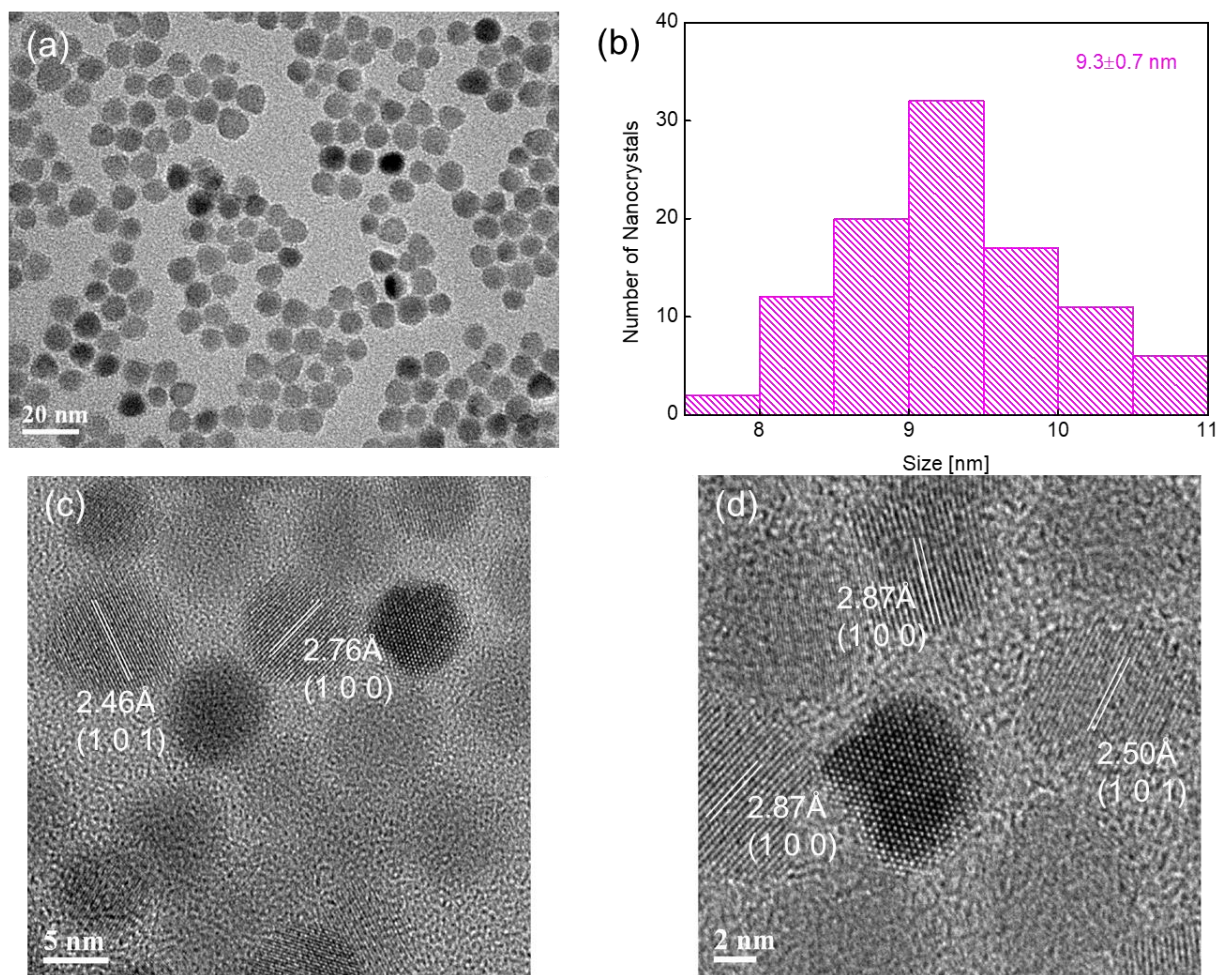
Figure 4.2 (a) Low-resolution overview TEM image, (b) The size distribution, (c), (d) High-resolution TEM images with measured lattice spacing of ZnO NCs synthesized under hydrogen (7 % H_2 in N_2) atmosphere.
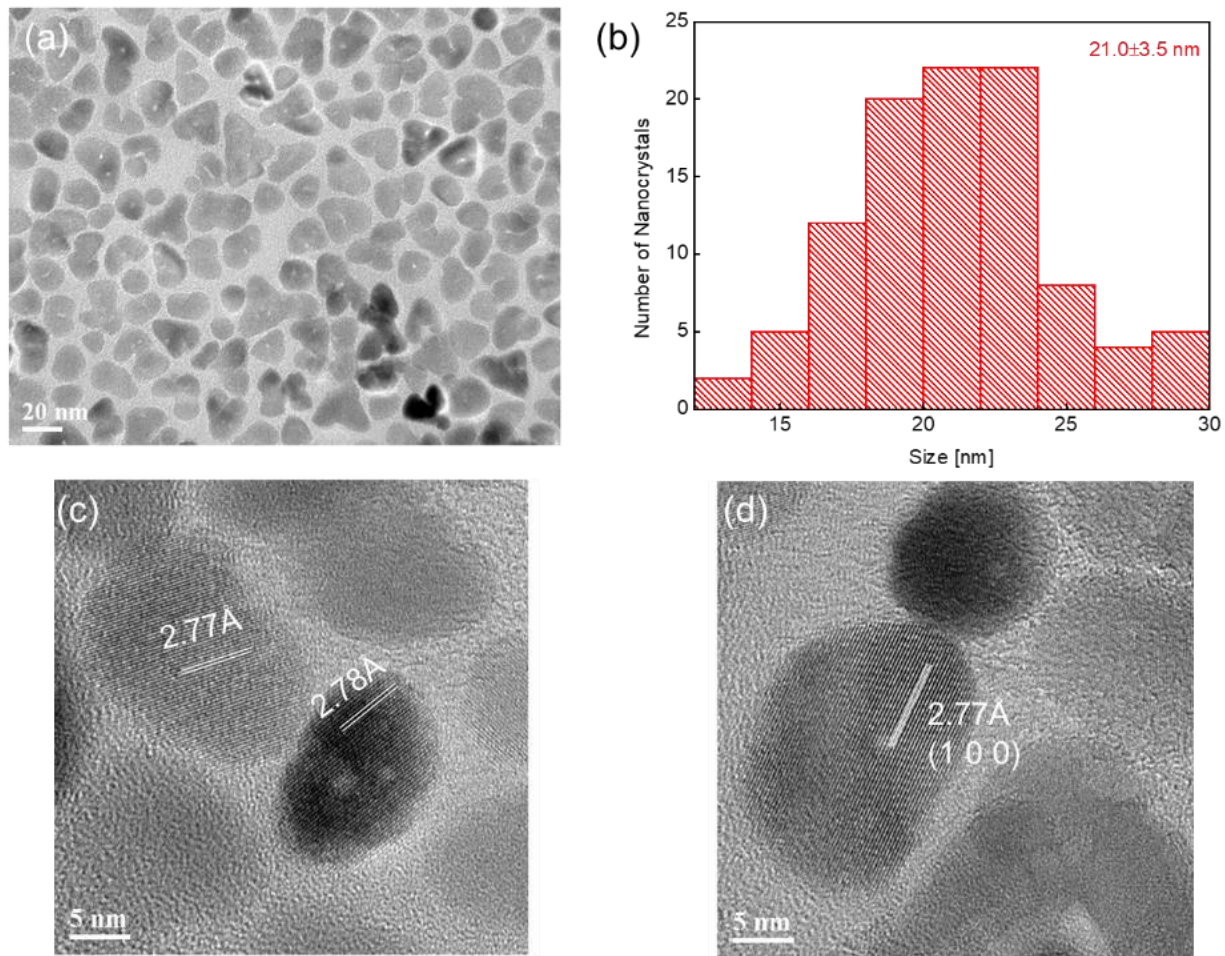
Figure 4.3 (a) Low-resolution overview TEM image, (b) The size distribution, (c) and (d) High-resolution TEM images with measured lattice spacing of ZnO NCs synthesized under air atmosphere, respectively.

4.1.2 Spectroscopic studies of ZnO NCs

UV-Vis absorption spectra of ZnO NCs were collected to obtain the absorption and calculate approximate optical band gap using Tauc plot (Equation 3.1) with n = 2 for direct bandgap semiconductors. Figure 4.4a illustrates the Tauc plots of ZnO NCs and resulting approximate

optical bandgap energy. The sizes in TEM images reveal that the size of ZnO NC samples are much larger than the exitonic Bohr radius of bulk ZnO, $a_B = 2.34$ nm,[96] so no quantum confinement effect is expected. ZnO NCs prepared under air atmosphere have the lowest bandgap energy because the oxidizing atmosphere can reduce the probability of oxygen vacancy formation and minimize their concentration. The synthesis under N_2 and Ar produce ZnO NCs with similar bandgap energy due to relative high defect concentration allowed by the presence of an inert gas. For hydrogen synthesized ZnO NCs, the reducing atmosphere increases probability to form oxygen vacancies due to deficiency of oxygen, leading to the highest bandgap energy among all samples.

PL emission spectra were collected to detect the concentration of defects in ZnO NCs. In Figure 4.4b, a broad green emission peak centered at 500 nm is observed for ZnO NCs, and the peak position does not shift as synthesis atmosphere changes. The visible emission peak at 500 nm (2.48 eV) is defect-related emission. According to Liao et al.[81], this visible emission could be due to the combination of singly ionized oxygen vacancies (V_O^+) and neutral oxygen vacancies (V_O^X) as indicated in Figure 1.15[81] originating from the combination of electrons on these shallow donor states and holes in the valence band. More importantly, the PL emission intensity trend (Figure 4.4b) concurs with the trend of optical bandgap energy. Peak intensities from high to low correspond to ZnO NCs obtained from H_2, Ar, N_2, and air, respectively. The change in PL emission intensity is originated from varying concentration of oxygen vacancies formed in the NCs under different atmosphere.
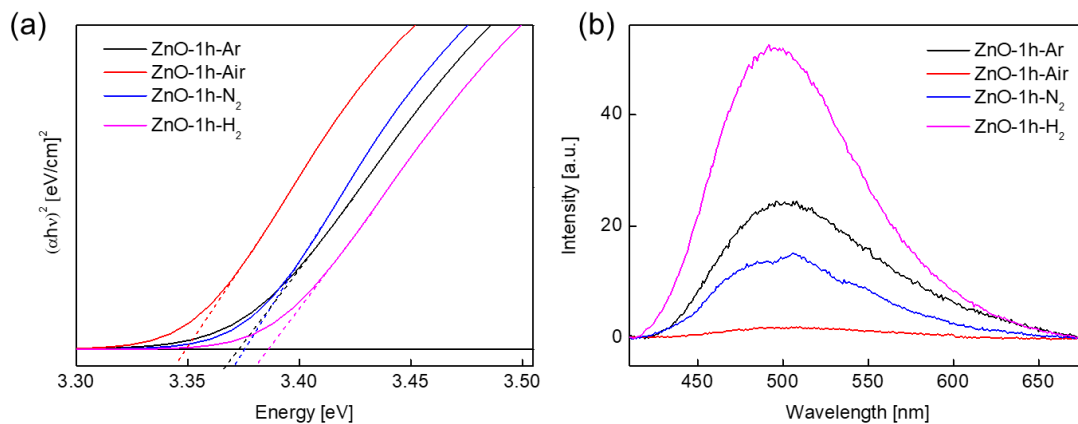
Figure 4.4 (a) Tauc plots of the optical band gap for ZnO NCs synthesized under various atmosphere. (b) PL emission spectra of ZnO NCs synthesized under various atmosphere using the excitation wavelength of 350 nm.

FTIR measurements were performed to investigate plasmonic properties of ZnO NCs prepared under different atmospheres and the spectra are shown in Figure 4.5. All FTIR spectra were normalized at Zn-O stretch peak (around 450 cm^{-1}). The peaks at 2924 cm^{-1} and 2824 cm^{-1} are attributed to CH_2 asymmetric and symmetric stretch of oleic acid, while the other two peaks at 1566 cm^{-1} and 1467 cm^{-1} are attributed to the COO- band stretch (formed during the reaction of $ZnSt_2$ and $In(acac)_3$ with DDOL). These suggest the presence of organic ligands on the surface of NCs. The characteristic LSPR broad peak is difficult to discern in the MIR range for these samples due to the insufficient free carrier concentration. However, for H_2-synthesized ZnO NCs, a slight slope towards FIR range can be observed indicating the possibility of the presence of a significantly broadened peak centered at FIR region and starting

from MIR region. So it would be necessary to collect FIR absorption spectra of these ZnO NCs in the future for confirmation of plasmonic properties.
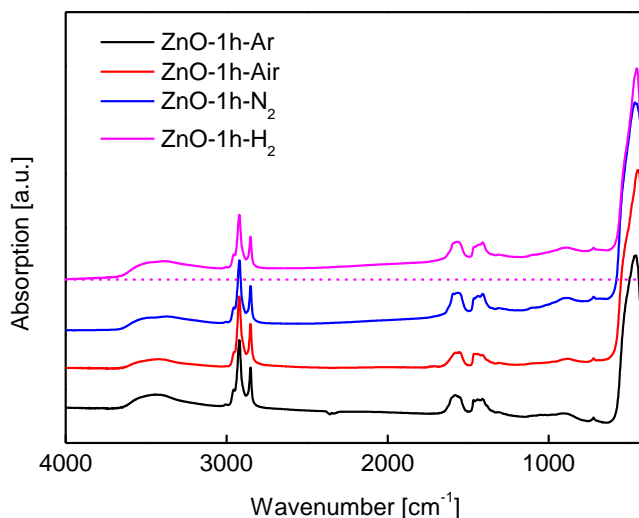
Figure 4.5 FTIR absorption spectra of ZnO NCs synthesized under various atmosphere (Ar, Air, N_2 and 7% H_2 in N_2).

4.1.3 Magneto-optical Properties of ZnO NCs

MCD spectroscopy has been broadly used in plasmonic semiconductor NCs, the key features of LSPR MCD responses are the linear field dependence and temperature independence.[53,54] Recently, these two features were also observed in plasmonic degenerately doped In_2O_3 NCs in the bandgap region, which provides an opportunity for the study of interface-free plasmon-exciton coupling in single-phase plasmonic metal oxide NCs.[56] MCD measurements were also performed to investigate the role of defect in the magneto-optical responses of ZnO NCs.

Figure 4.6a-c shows the absorption spectrum collected at 5 K and MCD spectra collected at various magnetic fields and various temperatures around the bandgap region of hydrogen-synthesized ZnO NCs. It can be observed that there is a derivative-shaped signal coinciding with the bandgap absorption transition, indicating excitonic splitting in these NCs. In Figure 4.6d, the integrated MCD intensity is plotted as a function of magnetic field strength showing a saturation at high magnetic fields characteristic for paramagnetic materials. The Brillouin function was fitted very well to the experimental data points for spin state S=1/2, which indicates the splitting is caused by the localized unpaired electrons associated with defects like oxygen vacancies.[58,97] Regarding the temperature dependence of MCD intensities, they reduce significantly with temperature from 5 to 50 K, and then decrease slowly until 300 K. The excellent Curie's law fitting of integrated MCD intensities with respect to temperature suggests the paramagnetic behavior of unpaired localized electrons in hydrogen-synthesized ZnO NCs.
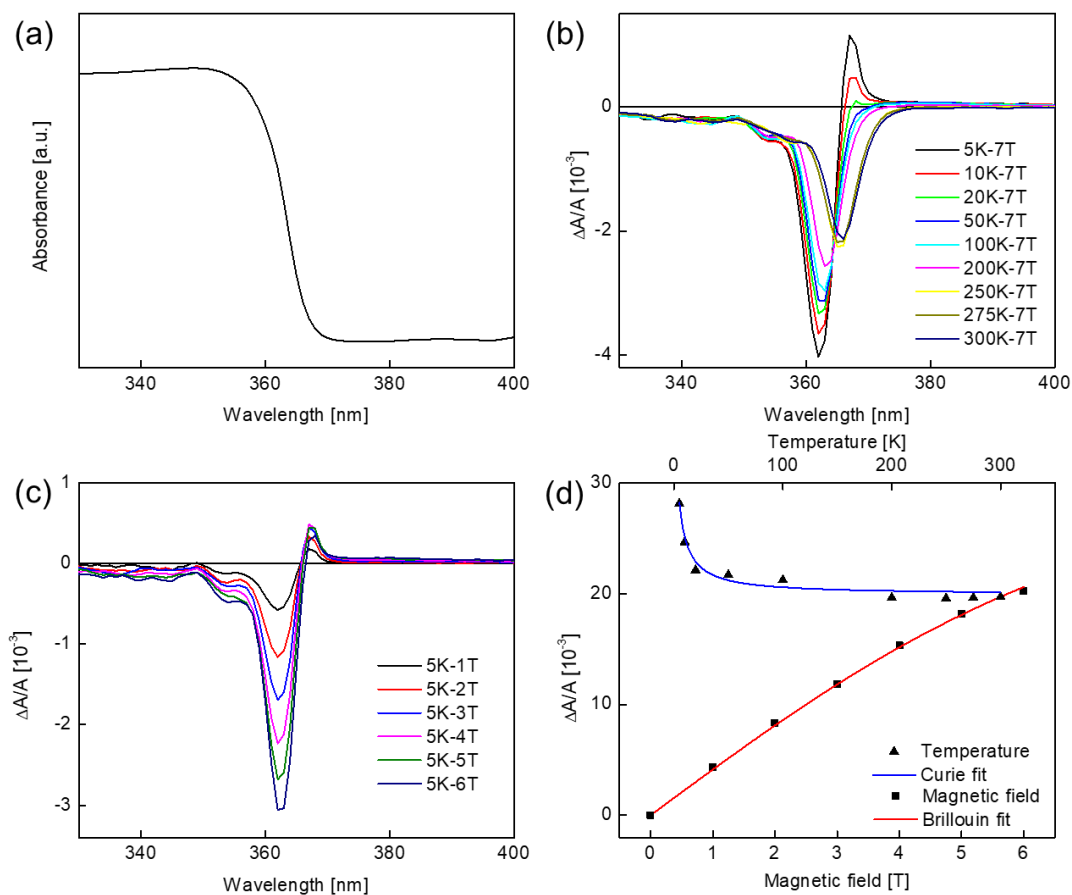
Figure 4.6 (a) Absorption spectra and (c) MCD spectra collected at 5 K for different external magnetic field strengths of ZnO NCs synthesized under hydrogen (7% H_2 in N_2). (b) MCD spectra of ZnO NCs synthesized under hydrogen collected at 7 T for various temperatures. (d) Magnetic field dependence and temperature dependence of integrated MCD intensity for ZnO NCs synthesized under hydrogen in (b) and (c) as functions of temperature and external magnetic field strength, respectively. Red solid line is the Brillouin function fit of the square data points. Blue solid line is fit to the Curie's law of triangle data points.

69

The MCD measurements were carried out for air synthesized ZnO NCs as well. The MCD spectra show a strong negative band which also coincides with the band edge absorption transition of the ZnO NCs (Figure 4.7). However, Curie-type decay is not observed in the temperature dependence of the MCD signal (Figure 4.7 inset), indicating a decreased amount of unpaired localized electrons due to the decreased oxygen vacancies in the oxidizing atmosphere. Together with PL spectra, these results show the Curie-type decay could be adjusted by defect manipulation via adjusting synthesizing atmosphere of ZnO NCs. The results of this work demonstrate for the first time that localized electrons associated with oxygen vacancies in ZnO NCs can lead to NC band splitting and carrier polarization without the necessity to incorporate magnetic dopants. To further confirm this assumption, the magnesium (Mg) dopant was introduced into ZnO NC lattice to study the correlation between defect manipulation and magneto-optics, some of the preliminary results are in the following section.
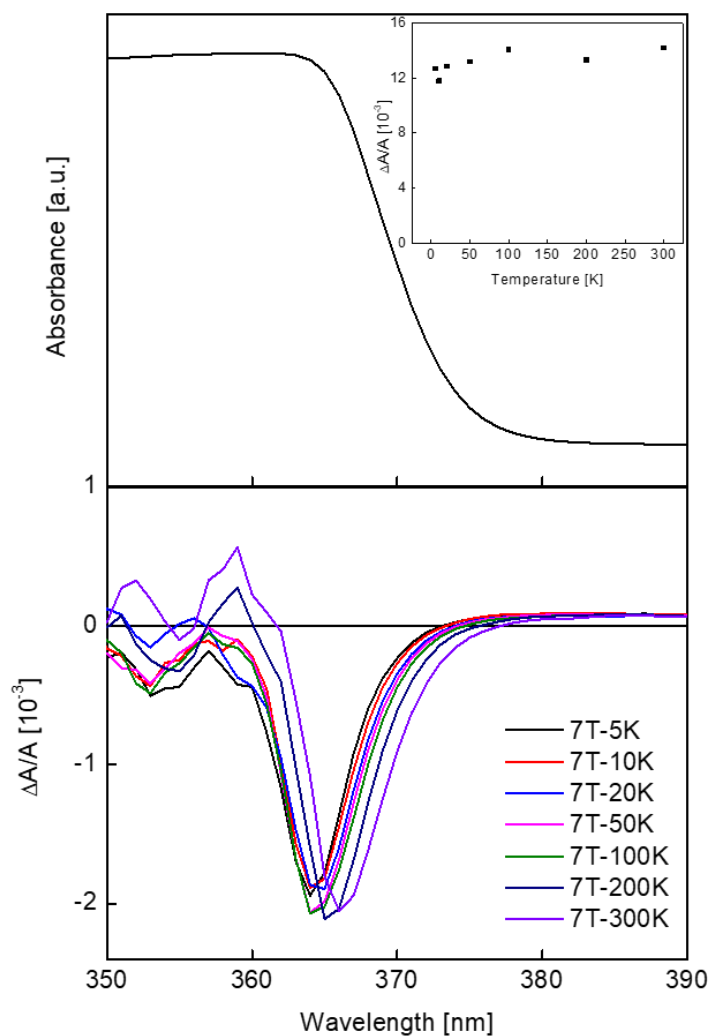
Figure 4.7 Absorption spectra (top panel) and MCD spectra of ZnO NCs synthesized under air collected at 7 T for various temperatures (bottom panel). Temperature dependence of integrated MCD intensity for ZnO NCs synthesized under air as a function of temperature (inset).

71

4.2 Magnesium-doped ZnO NCs

4.2.1 Crystal structure and morphology of Mg-doped ZnO NCs

Figure 4.8 depicts the XRD patterns of pure ZnO and Mg-doped ZnO NCs (MZO) with different doping concentration up to 20%. There is no peak relating impurity observed for all Mg-doped samples indicating the substitution of Mg ion caused little lattice distortion in the wurtzite structure of ZnO due to the close ionic radii of Mg (0.57 Å) and Zn (0.60 Å).[98] The XRD peaks get broader when the doping concentration increases, suggesting the smaller sizes are obtained with a high doping level. This reveals that the presence of Mg ions in ZnO may inhibit the crystal growth. As observed in XRD patterns, all MZO NCs show the preferred growing orientation of (002) as the corresponding peak is more pronounced with increasing doping concentration. This preferred growing orientation can also be observed in high-resolution TEM images (Figure 4.9d) of 10% MZO NCs with average measured lattice spacing of 2.50 Å and 2.60 Å, which are corresponding to (101) and (002) planes, respectively. There are more (002) planes observed for 10 % MZO NCs compared with pure ZnO NCs (Figure 4.2, 4.3). The low-resolution TEM images in Figure 4.9a and b show that the 10% MZO NCs are uniformly distributed with cone-like shapes. The average NC size is 11.7 ± 1.3 nm (Figure 4.9c). The actual doping concentration of 10% MZO NCs is 9.07% obtained from energy dispersive X-Ray analysis (EDX) of TEM, suggesting an efficient doping process.
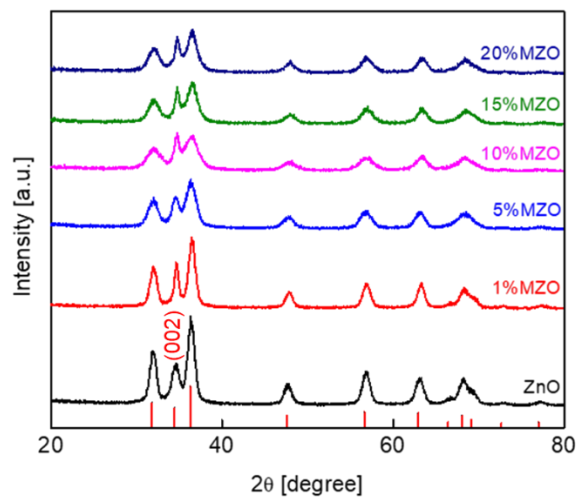
Figure 4.8 XRD patterns of Mg-doped ZnO NCs with varying doping concentration.
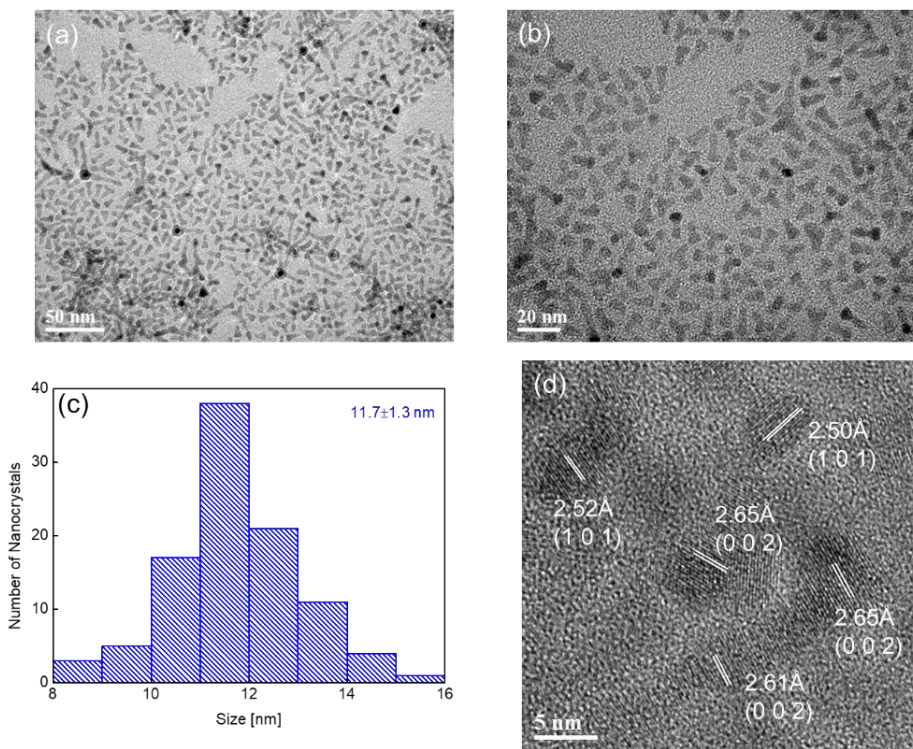
Figure 4.9 (a) (b) Low-resolution overview TEM images, (c) The size distribution, (d) High-resolution TEM images with measured lattice spacing of 10 % Mg-doped ZnO NCs.

4.2.2 Spectroscopic studies of Mg-doped ZnO NCs

The UV-vis spectroscopy measurements were conducted to estimate the optical bandgap energy of MZO NCs. The Tauc plots obtained from UV-vis spectra are shown in Figure 4.10a. The optical bandgap energy increases as doping concentration increases up to 10% and then decreases with higher doping concentration. The increase of optical band gap energy with Mg doping level can be attributed to the Burstein-Moss effect caused by electrons introduced by oxygen vacancies.[99] Substitution of Zn ion by Mg can increase the oxygen vacancies and consequent electron density because Mg atom loses electrons more easily than Zn atom due to the lower electronegativity of Mg (1.31) compared with Zn (1.65).[100] It also reveals the ability of Mg ion to change the electronic structure of ZnO NCs. The drop of optical bandgap energy at high Mg-content may be attributed to the trapping sites of Mg ion or electron scattering effect.[5] Figure 4.10b shows the PL spectra of MZO NCs at room temperature. These Mg-doped samples also have characteristic defect-related visible emission of ZnO NCs but with high intensities. As the doping concentration increases to 15%, the PL emission becomes stronger due to the increased concentration of oxygen vacancies.

In terms of plasmonic properties of MZO NCs, the characteristic broad peak is not observed in the UV-vis-NIR range (200-3300 nm) for 5%, 10%, 15% and 20% Mg-doped samples (Figure 4.10c). However, a slope similar with ZnO NCs prepared under hydrogen atmosphere can be observed for 10% MZO (Figure 4.10d) indicating the possibility of existence of plasmonic peak centered in the FIR range with an extension to MIR region. The plasmonic properties in the FIR range need to be further investigated.
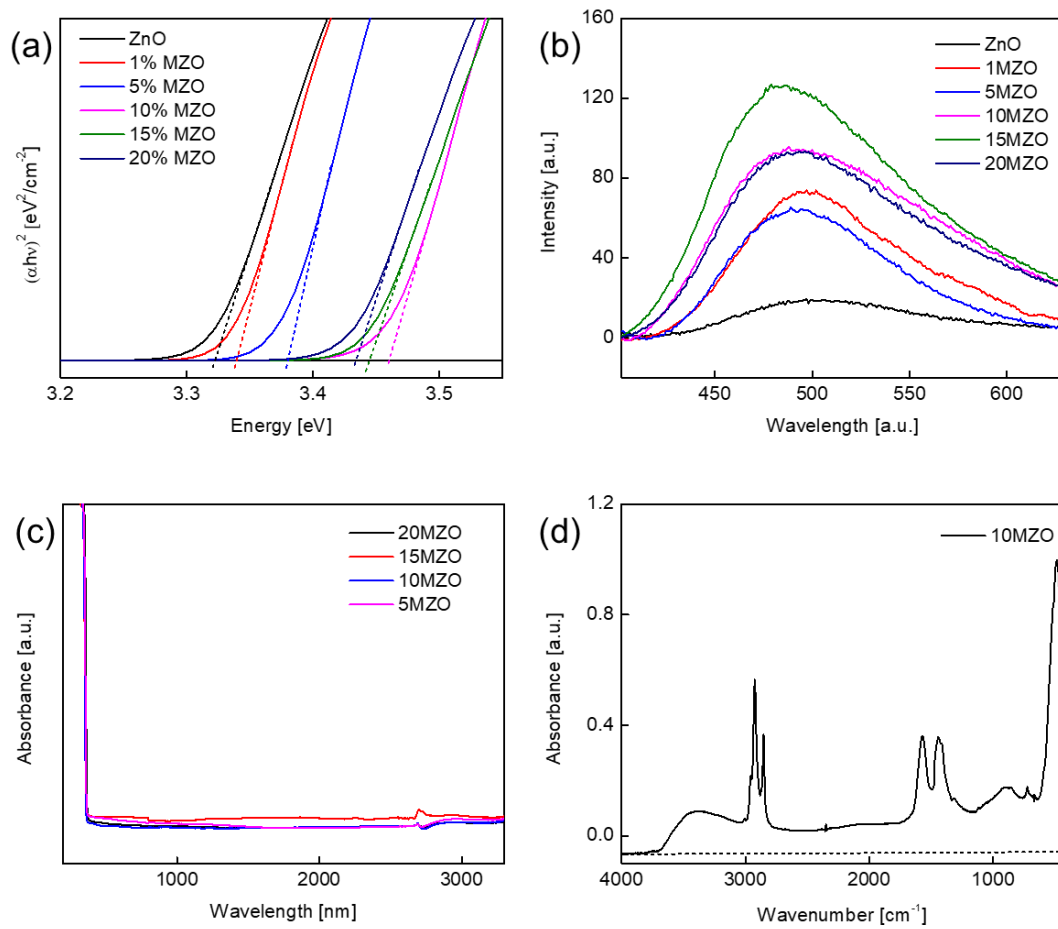
Figure 4.10 (a) Tauc plots obtained from UV-vis spectra (b) Room temperature PL spectra using 325 nm excitation wavelength of pure and Mg-doped samples. (c) UV-vis-NIR absorbance spectra of Mg-doped ZnO NCs. (d) FTIR absorbance spectra of 10% Mg-doped ZnO NCs.

4.3 Conclusions

In this chapter, pure and Mg-doped ZnO NCs were successfully synthesized with uniform size distribution. Pure ZnO NCs exhibit quasi-spherical shape whereas MZO NCs are in the shape of cones due to effect of Mg dopant. For pure ZnO NCs synthesized under different atmosphere, the oxidizing atmosphere (air) tends to saturate oxygen vacancies leading to a small bandgap energy and weak PL emission. On the contrary, the reducing atmosphere (hydrogen) can increase the possibility of generating oxygen vacancies due to the oxygen-deficient environment leading to high bandgap energy and strong PL emission. The inert atmosphere (argon and nitrogen) tends to give NCs moderate amount of oxygen vacancies. As indicated by PL spectra, the defect concentration is successfully manipulated by tuning synthesis atmosphere. More importantly, the Curie-type decay associated with unpaired localized electrons introduced by these defects can also be manipulated by controlling defect concentration as indicated by MCD spectra. For MZO NCs, the defect concentration is further manipulated by doping ZnO NCs with Mg ion. The bandgap energy is blue-shifted and PL emission is much stronger in contrast to pure ZnO NCs suggesting the increased amount of oxygen vacancies due to the electronegativity difference. The defect-correlated band splitting monitored by MCD spectroscopy in MZO NCs would be an intriguing topic to be further studied. The ability to control exciton polarization in pure ZnO NCs using individual (localized) electrons enable the potential technological applications including spintronics and quantum information processing.

Chapter 5

Future work

In this work, we investigated the photo-thermal catalytic reactions of WO_{3-x} NCs in the dark. However, photocatalytic reactions under IR light irradiation with various monoclinic wavelength will give a more detailed look on the relationship between photocatalytic performance and the characteristic LSPR absorption, which represents a rich area for future research. Additionally, Brunauer-Emmett-Teller (BET) analysis technique should be used for the measurement of specific surface area of WO_{3-x} NCs. The valence band maximum and conduction band minimum of WO_{3-x} NCs is also worthwhile to be explored using ultraviolet photoelectron spectroscopy (UPS) to determine the band positions relative to NHE. Furthermore, an important question that arises from this work is if WO_{3-x} NCs can be used in photocatalytic water splitting process to obtain hydrogen as a green energy resources with zero pollution produced. In a long term, other plasmonic semiconductor NCs can be designed and applied in photocatalysis process.

Regarding the study on magneto-optical properties of ZnO NCs, the MCD spectroscopy measurements have been done on the pure ZnO NCs prepared under air and hydrogen showing a defect-correlated Curie type decay caused by unpaired localized electrons. Since the MZO NCs exhibit stronger PL emission than pure ZnO NCs, the defect-correlated band splitting of MZO NCs investigated by MCD spectroscopy would be an intriguing topic to be further

77

studied. We can also extend the generality of defect-correlated band splitting in other plasmonic semiconductor NCs.

Bibliography

(1)   Atwater, H. A.; Polman, A. Plasmonics for Improved Photovoltaic Devices. *Nat. Mater.* **2010**, *9* (3), 205–213.

(2)   Zhang, X.; Chen, Y. L.; Liu, R.-S.; Tsai, D. P. Plasmonic Photocatalysis. *Rep. Prog. Phys.* **2013**, *76* (4), 046401.

(3)   Anker, J. N.; Hall, W. P.; Lyandres, O.; Shah, N. C.; Zhao, J.; Van Duyne, R. P. Biosensing with Plasmonic Nanosensors. *Nat. Mater.* **2008**, *7* (6), 442–453.

(4)   Mayer, K. M.; Hafner, J. H. Localized Surface Plasmon Resonance Sensors. *Chem. Rev.* **2011**, *111* (6), 3828–3857.

(5)   Agrawal, A.; Cho, S. H.; Zandi, O.; Ghosh, S.; Johns, R. W.; Milliron, D. J. Localized Surface Plasmon Resonance in Semiconductor Nanocrystals. *Chem. Rev.* **2018**, *118* (6), 3121–3207.

(6)   Faucheaux, J. A.; Stanton, A. L. D.; Jain, P. K. Plasmon Resonances of Semiconductor Nanocrystals: Physical Principles and New Opportunities. *J. Phys. Chem. Lett.* **2014**, *5* (6), 976–985.

(7)   Buonsanti, R.; Llordes, A.; Aloni, S.; Helms, B. A.; Milliron, D. J. Tunable Infrared Absorption and Visible Transparency of Colloidal Aluminum-Doped Zinc Oxide Nanocrystals. *Nano Lett.* **2011**, *11* (11), 4706–4710.

(8)   Manthiram, K.; Alivisatos, A. P. Tunable Localized Surface Plasmon Resonances in Tungsten Oxide Nanocrystals. *J. Am. Chem. Soc.* **2012**, *134* (9), 3995–3998.

(9)   Gordon, T. R.; Paik, T.; Klein, D. R.; Naik, G. V.; Caglayan, H.; Boltasseva, A.; Murray,

C. B. Shape-Dependent Plasmonic Response and Directed Self-Assembly in a New Semiconductor Building Block, Indium-Doped Cadmium Oxide (ICO). *Nano Lett.* **2013**, *13* (6), 2857–2863.

(10) Kanehara, M.; Koike, H.; Yoshinaga, T.; Teranishi, T. Indium Tin Oxide Nanoparticles with Compositionally Tunable Surface Plasmon Resonance Frequencies in the Near-IR Region. *J. Am. Chem. Soc.* **2009**, *131* (49), 17736–17737.

(11) Fang, H.; Hegde, M.; Yin, P.; Radovanovic, P. V. Tuning Plasmon Resonance of In_2O_3 Nanocrystals throughout the Mid-Infrared Region by Competition between Electron Activation and Trapping. *Chem. Mater.* **2017**, *29* (11), 4970–4979.

(12) Coughlan, C.; Ibáñez, M.; Dobrozhan, O.; Singh, A.; Cabot, A.; Ryan, K. M. Compound Copper Chalcogenide Nanocrystals. *Chem. Rev.* **2017**, *117* (9), 5865–6109.

(13) Crockett, B. M.; Jansons, A. W.; Koskela, K. M.; Sharps, M. C.; Johnson, D. W.; Hutchison, J. E. Influence of Nanocrystal Size on the Optoelectronic Properties of Thin, Solution-Cast Sn-Doped In_2O_3 Films. *Chem. Mater.* **2019**, *31* (9), 3370–3380.

(14) Della Gaspera, E.; Chesman, A. S. R.; van Embden, J.; Jasieniak, J. J. Non-Injection Synthesis of Doped Zinc Oxide Plasmonic Nanocrystals. *ACS Nano* **2014**, *8* (9), 9154–9163.

(15) Luther, J. M.; Jain, P. K.; Ewers, T.; Alivisatos, A. P. Localized Surface Plasmon Resonances Arising from Free Carriers in Doped Quantum Dots. *Nat. Mater.* **2011**, *10* (5), 361–366.

(16) Lounis, S. D.; Runnerstrom, E. L.; Llordés, A.; Milliron, D. J. Defect Chemistry and

Plasmon Physics of Colloidal Metal Oxide Nanocrystals. *J. Phys. Chem. Lett.* **2014**, *5* (9), 1564–1574.

(17)   Li, Y.; Cheng, J.; Liu, Y.; Liu, P.; Cao, W.; He, T.; Chen, R.; Tang, Z. Manipulation of Surface Plasmon Resonance in Sub-Stoichiometry Molybdenum Oxide Nanodots through Charge Carrier Control Technique. *J. Phys. Chem. C* **2017**, *121* (9), 5208–5214.

(18)   Kriegel, I.; Scotognella, F.; Manna, L. Plasmonic Doped Semiconductor Nanocrystals: Properties, Fabrication, Applications and Perspectives. *Phys. Rep.* **2017**, *674*, 1–52.

(19)   Wang, T.; Radovanovic, P. V. Free Electron Concentration in Colloidal Indium Tin Oxide Nanocrystals Determined by Their Size and Structure. *J. Phys. Chem. C* **2011**, *115* (2), 406–413.

(20)   Comin, A.; Manna, L. New Materials for Tunable Plasmonic Colloidal Nanocrystals. *Chem. Soc. Rev.* **2014**, *43* (11), 3957–3975.

(21)   L. Runnerstrom, E.; Llordés, A.; D. Lounis, S.; J. Milliron, D. Nanostructured Electrochromic Smart Windows: Traditional Materials and NIR-Selective Plasmonic Nanocrystals. *Chem. Commun.* **2014**, *50* (73), 10555–10572.

(22)   Zhong, Y.; Malagari, S. D.; Hamilton, T.; Wasserman, D. M. Review of Mid-Infrared Plasmonic Materials. *J. Nanophotonics* **2015**, *9* (1), 093791.

(23)   Naik, G. V.; Shalaev, V. M.; Boltasseva, A. Alternative Plasmonic Materials: Beyond Gold and Silver. *Adv. Mater.* **2013**, *25* (24), 3264–3294.

(24)   Niezgoda, J. S.; Rosenthal, S. J. Synthetic Strategies for Semiconductor Nanocrystals Expressing Localized Surface Plasmon Resonance. *ChemPhysChem* **2016**, *17* (5), 645–

653.

(25)   Ye, X.; Fei, J.; Diroll, B. T.; Paik, T.; Murray, C. B. Expanding the Spectral Tunability of Plasmonic Resonances in Doped Metal-Oxide Nanocrystals through Cooperative Cation-Anion Codoping. *J. Am. Chem. Soc.* **2014**, *136* (33), 11680–11686.

(26)   Tandon, B.; Yadav, A.; Khurana, D.; Reddy, P.; Santra, P. K.; Nag, A. Size-Induced Enhancement of Carrier Density, LSPR Quality Factor, and Carrier Mobility in Cr–Sn Doped In_2O_3 Nanocrystals. *Chem. Mater.* **2017**, *29* (21), 9360–9368.

(27)   Fujishima, A.; Honda, K. Electrochemical Photolysis of Water at a Semiconductor Electrode. *Nature* **1972**, *238* (5358), 37–38.

(28)   Chen, C.; Ma, W.; Zhao, J. Semiconductor-Mediated Photodegradation of Pollutants under Visible-Light Irradiation. *Chem. Soc. Rev.* **2010**, *39* (11), 4206–4219.

(29)   Daneshvar, N.; Salari, D.; Khataee, A. R. Photocatalytic Degradation of Azo Dye Acid Red 14 in Water on ZnO as an Alternative Catalyst to TiO_2. *J. Photochem. Photobiol. Chem.* **2004**, *162* (2), 317–322.

(30)   Ahmad, H.; Kamarudin, S. K.; Minggu, L. J.; Kassim, M. Hydrogen from Photo-Catalytic Water Splitting Process: A Review. *Renew. Sustain. Energy Rev.* **2015**, *43*, 599–610.

(31)   Zhang, X.; Chen, Y. L.; Liu, R.-S.; Tsai, D. P. Plasmonic Photocatalysis. *Rep. Prog. Phys.* **2013**, *76* (4), 046401.

(32)   Wu, N. Plasmonic Metal–Semiconductor Photocatalysts and Photoelectrochemical Cells: A Review. *Nanoscale* **2018**, *10* (6), 2679–2696.

(33) Awazu, K.; Fujimaki, M.; Rockstuhl, C.; Tominaga, J.; Murakami, H.; Ohki, Y.; Yoshida, N.; Watanabe, T. A Plasmonic Photocatalyst Consisting of Silver Nanoparticles Embedded in Titanium Dioxide. *J. Am. Chem. Soc.* **2008**, *130* (5), 1676–1680.

(34) Gomes Silva, C.; Juárez, R.; Marino, T.; Molinari, R.; García, H. Influence of Excitation Wavelength (UV or Visible Light) on the Photocatalytic Activity of Titania Containing Gold Nanoparticles for the Generation of Hydrogen or Oxygen from Water. *J. Am. Chem. Soc.* **2011**, *133* (3), 595–602.

(35) Lian, Z.; Sakamoto, M.; Vequizo, J. J. M.; Ranasinghe, C. S. K.; Yamakata, A.; Nagai, T.; Kimoto, K.; Kobayashi, Y.; Tamai, N.; Teranishi, T. Plasmonic p–n Junction for Infrared Light to Chemical Energy Conversion. *J. Am. Chem. Soc.* **2019**, *141* (6), 2446–2450.

(36) Zhang, Z.; Huang, J.; Fang, Y.; Zhang, M.; Liu, K.; Dong, B. A Nonmetal Plasmonic Z-Scheme Photocatalyst with UV- to NIR-Driven Photocatalytic Protons Reduction. *Adv. Mater.* **2017**, *29* (18), 1606688.

(37) Gan, X. Y.; Keller, E. L.; Warkentin, C. L.; Crawford, S. E.; Frontiera, R. R.; Millstone, J. E. Plasmon-Enhanced Chemical Conversion Using Copper Selenide Nanoparticles. *Nano Lett.* **2019**, *19* (4), 2384–2388.

(38) Paik, T.; Cargnello, M.; Gordon, T. R.; Zhang, S.; Yun, H.; Lee, J. D.; Woo, H. Y.; Oh, S. J.; Kagan, C. R.; Fornasiero, P.; Murray, C. B. Photocatalytic Hydrogen Evolution from Substoichiometric Colloidal WO_{3-x} Nanowires. *ACS Energy Lett.* **2018**, *3* (8), 1904–1910.

(39) Ohno, H. Making Nonmagnetic Semiconductors Ferromagnetic. *Science* **1998**, *281* (5379), 951–956.

(40) Furdyna, J. K. Diluted Magnetic Semiconductors. *J. Appl. Phys.* **1988**, *64* (4), R29–R64.

(41) Coey, J. M. D.; Venkatesan, M.; Fitzgerald, C. B. Donor Impurity Band Exchange in Dilute Ferromagnetic Oxides. *Nat. Mater.* **2005**, *4* (2), 173–179.

(42) Radovanovic, P. V.; Gamelin, D. R. High-Temperature Ferromagnetism in Ni^{2+}-Doped ZnO Aggregates Prepared from Colloidal Diluted Magnetic Semiconductor Quantum Dots. *Phys. Rev. Lett.* **2003**, *91* (15), 157202.

(43) Lee, H.-J.; Jeong, S.-Y.; Cho, C. R.; Park, C. H. Study of Diluted Magnetic Semiconductor: Co-Doped ZnO. *Appl. Phys. Lett.* **2002**, *81* (21), 4020–4022.

(44) Bryan, J. D.; Heald, S. M.; Chambers, S. A.; Gamelin, D. R. Strong Room-Temperature Ferromagnetism in Co^{2+}-Doped TiO_2 Made from Colloidal Nanocrystals. *J. Am. Chem. Soc.* **2004**, *126* (37), 11640–11647.

(45) Archer, P. I.; Radovanovic, P. V.; Heald, S. M.; Gamelin, D. R. Low-Temperature Activation and Deactivation of High-Curie-Temperature Ferromagnetism in a New Diluted Magnetic Semiconductor: Ni^{2+}-Doped SnO_2. *J. Am. Chem. Soc.* **2005**, *127* (41), 14479–14487.

(46) Sabergharesou, T.; Wang, T.; Ju, L.; Radovanovic, P. V. Electronic Structure and Magnetic Properties of Sub-3 Nm Diameter Mn-Doped SnO_2 Nanocrystals and Nanowires. *Appl. Phys. Lett.* **2013**, *103* (1), 012401.

(47) Farvid, S. S.; Hegde, M.; Radovanovic, P. V. Influence of the Host Lattice Electronic

Structure on Dilute Magnetic Interactions in Polymorphic Cr (III)-Doped In_2O_3 Nanocrystals. *Chem. Mater.* **2013**, *25* (2), 233–244.

(48) Farvid, S. S.; Sabergharesou, T.; Hutfluss, L. N.; Hegde, M.; Prouzet, E.; Radovanovic, P. V. Evidence of Charge-Transfer Ferromagnetism in Transparent Diluted Magnetic Oxide Nanocrystals: Switching the Mechanism of Magnetic Interactions. *J. Am. Chem. Soc.* **2014**, *136* (21), 7669–7679.

(49) Hu, S.; Yan, S.; Lin, X.; Yao, X.; Chen, Y.; Liu, G.; Mei, L. Electronic Structure of Fe-Doped In_2O_3 Magnetic Semiconductor with Oxygen Vacancies: Evidence for F-Center Mediated Exchange Interaction. *Appl. Phys. Lett.* **2007**, *91* (26), 262514.

(50) Xing, P. F.; Chen, Y. X.; Yan, S.-S.; Liu, G. L.; Mei, L. M.; Zhang, Z. Tunable Ferromagnetism by Oxygen Vacancies in Fe-Doped In_2O_3 Magnetic Semiconductor. *J. Appl. Phys.* **2009**, *106* (4), 043909.

(51) Pineider, F.; de Julián Fernández, C.; Videtta, V.; Carlino, E.; al Hourani, A.; Wilhelm, F.; Rogalev, A.; Cozzoli, P. D.; Ghigna, P.; Sangregorio, C. Spin-Polarization Transfer in Colloidal Magnetic-Plasmonic Au/Iron Oxide Hetero-Nanocrystals. *ACS Nano* **2013**, *7* (1), 857–866.

(52) Armelles, G.; Cebollada, A.; García-Martín, A.; González, M. U. Magnetoplasmonics: Combining Magnetic and Plasmonic Functionalities. *Adv. Opt. Mater.* **2013**, *1* (1), 10–35.

(53) Schimpf, A. M.; Thakkar, N.; Gunthardt, C. E.; Masiello, D. J.; Gamelin, D. R. Charge-Tunable Quantum Plasmons in Colloidal Semiconductor Nanocrystals. *ACS Nano* **2014**,

8 (1), 1065–1072.

(54) Schimpf, A. M.; Lounis, S. D.; Runnerstrom, E. L.; Milliron, D. J.; Gamelin, D. R. Redox Chemistries and Plasmon Energies of Photodoped In_2O_3 and Sn-Doped In_2O_3 (ITO) Nanocrystals. *J. Am. Chem. Soc.* **2015**, *137* (1), 518–524.

(55) Pineider, F.; Campo, G.; Bonanni, V.; de Julián Fernández, C.; Mattei, G.; Caneschi, A.; Gatteschi, D.; Sangregorio, C. Circular Magnetoplasmonic Modes in Gold Nanoparticles. *Nano Lett.* **2013**, *13* (10), 4785–4789..

(56) Yin, P.; Tan, Y.; Fang, H.; Hegde, M.; Radovanovic, P. V. Plasmon-Induced Carrier Polarization in Semiconductor Nanocrystals. *Nat. Nanotechnol.* **2018**, *13* (6), 463–467.

(57) Ando, K. MATERIALS SCIENCE: Seeking Room-Temperature Ferromagnetic Semiconductors. *Science* **2006**, *312* (5782), 1883–1885.

(58) Yin, P.; Hegde, M.; Tan, Y.; Chen, S.; Garnet, N.; Radovanovic, P. V. Controlling the Mechanism of Excitonic Splitting in In_2O_3 Nanocrystals by Carrier Delocalization. *ACS Nano* **2018**, *12* (11), 11211–11218.

(59) Hartstein, K. H.; Schimpf, A. M.; Salvador, M.; Gamelin, D. R. Cyclotron Splittings in the Plasmon Resonances of Electronically Doped Semiconductor Nanocrystals Probed by Magnetic Circular Dichroism Spectroscopy. *J. Phys. Chem. Lett.* **2017**, *8* (8), 1831–1836.

(60) Mason, W. R. *Magnetic Circular Dichroism Spectroscopy*; John Wiley & Sons, **2007**.

(61) Han, B.; Gao, X.; Lv, J.; Tang, Z. Magnetic Circular Dichroism in Nanomaterials: New Opportunity in Understanding and Modulation of Excitonic and Plasmonic Resonances.

Adv. Mater. **2018**, 1801491.

(62) Woodward, P. M. Octahedral Tilting in Perovskites. I. Geometrical Considerations. *Acta Crystallogr. B* **1997**, *53* (1), 32–43.

(63) Zheng, H.; Ou, J. Z.; Strano, M. S.; Kaner, R. B.; Mitchell, A.; Kalantar-zadeh, K. Nanostructured Tungsten Oxide – Properties, Synthesis, and Applications. *Adv. Funct. Mater.* **2011**, *21* (12), 2175–2196.

(64) Thummavichai, K.; Wang, N.; Xu, F.; Rance, G.; Xia, Y.; Zhu, Y. In Situ Investigations of the Phase Change Behaviour of Tungsten Oxide Nanostructures. *R. Soc. Open Sci. 5* (4), 171932.

(65) Ramana, C. V.; Utsunomiya, S.; Ewing, R. C.; Julien, C. M.; Becker, U. Structural Stability and Phase Transitions in WO$_3$ Thin Films. *J. Phys. Chem. B* **2006**, *110* (21), 10430–10435.

(66) Huang, Z.-F.; Song, J.; Pan, L.; Zhang, X.; Wang, L.; Zou, J.-J. Tungsten Oxides for Photocatalysis, Electrochemistry, and Phototherapy. *Adv. Mater.* **2015**, *27* (36), 5309–5327.

(67) Frey, G. L.; Rothschild, A.; Sloan, J.; Rosentsveig, R.; Popovitz-Biro, R.; Tenne, R. Investigations of Nonstoichiometric Tungsten Oxide Nanoparticles. *J. Solid State Chem.* **2001**, *162* (2), 300–314.

(68) Liu, L.; Mei, Z.; Tang, A.; Azarov, A.; Kuznetsov, A.; Xue, Q.-K.; Du, X. Oxygen Vacancies: The Origin of n-Type Conductivity in ZnO. *Phys. Rev. B* **2016**, *93* (23), 235305.

(69) Jeem, M.; Zhang, L.; Ishioka, J.; Shibayama, T.; Iwasaki, T.; Kato, T.; Watanabe, S. Tuning Optoelectrical Properties of ZnO Nanorods with Excitonic Defects via Submerged Illumination. *Nano Lett.* **2017**, *17* (3), 2088–2093.

(70) Repp, S.; Weber, S.; Erdem, E. Defect Evolution of Nonstoichiometric ZnO Quantum Dots. *J. Phys. Chem. C* **2016**, *120* (43), 25124–25130.

(71) Camarda, P.; Messina, F.; Vaccaro, L.; Agnello, S.; Buscarino, G.; Schneider, R.; Popescu, R.; Gerthsen, D.; Lorenzi, R.; Mario Gelardi, F.; Cannas, M. Luminescence Mechanisms of Defective ZnO Nanoparticles. *Phys. Chem. Chem. Phys.* **2016**, *18* (24), 16237–16244.

(72) Wang, Z. L. Zinc Oxide Nanostructures: Growth, Properties and Applications. *J. Phys. Condens. Matter* **2004**, *16* (25), R829.

(73) Sirelkhatim, A.; Mahmud, S.; Seeni, A.; Kaus, N. H. M.; Ann, L. C.; Bakhori, S. K. M.; Hasan, H.; Mohamad, D. Review on Zinc Oxide Nanoparticles: Antibacterial Activity and Toxicity Mechanism. *Nano-Micro Lett.* **2015**, *7* (3), 219–242.

(74) Özgür, Ü.; Alivov, Ya. I.; Liu, C.; Teke, A.; Reshchikov, M. A.; Doğan, S.; Avrutin, V.; Cho, S.-J.; Morkoç, H. A Comprehensive Review of ZnO Materials and Devices. *J. Appl. Phys.* **2005**, *98* (4), 041301.

(75) Ong, C. B.; Ng, L. Y.; Mohammad, A. W. A Review of ZnO Nanoparticles as Solar Photocatalysts: Synthesis, Mechanisms and Applications. *Renew. Sustain. Energy Rev.* **2018**, *81*, 536–551.

(76) Janotti, A.; Van de Walle, C. G. Native Point Defects in ZnO. *Phys. Rev. B* **2007**, *76* (16),

165202.

(77)   Gsiea, A. M.; Goss, J. P.; Briddon, P. R.; Al-habashi, R. M.; Etmimi, K. M.; Marghani, K. A. S. Native Point Defects in ZnO. **2014**, *8* (1), 6.

(78)   Lin, B.; Fu, Z.; Jia, Y. Green Luminescent Center in Undoped Zinc Oxide Films Deposited on Silicon Substrates. *Appl. Phys. Lett.* **2001**, *79* (7), 943–945.

(79)   Barbagiovanni, E. G.; Strano, V.; Franzò, G.; Crupi, I.; Mirabella, S. Photoluminescence Transient Study of Surface Defects in ZnO Nanorods Grown by Chemical Bath Deposition. *Appl. Phys. Lett.* **2015**, *106* (9), 093108. https://doi.org/10.1063/1.4914067.

(80)   Børseth, T. M.; Svensson, B. G.; Kuznetsov, A. Yu.; Klason, P.; Zhao, Q. X.; Willander, M. Identification of Oxygen and Zinc Vacancy Optical Signals in ZnO. *Appl. Phys. Lett.* **2006**, *89* (26), 262112.

(81)   Liao, Z.-M.; Zhang, H.-Z.; Zhou, Y.-B.; Xu, J.; Zhang, J.-M.; Yu, D.-P. Surface Effects on Photoluminescence of Single ZnO Nanowires. *Phys. Lett. A* **2008**, *372* (24), 4505–4509.

(82)   Zhu, Q.; Xie, C.; Li, H.; Yang, C.; Zhang, S.; Zeng, D. Selectively Enhanced UV and NIR Photoluminescence from a Degenerate ZnO Nanorod Array Film. *J. Mater. Chem. C* **2014**, *2* (23), 4566–4580.

(83)   Smith, K. K. Photoluminescence of Semiconductor Materials. *Thin Solid Films* **1981**, *84* (2), 171–182.

(84)   Liu, D.; Lv, Y.; Zhang, M.; Liu, Y.; Zhu, Y.; Zong, R.; Zhu, Y. Defect-Related Photoluminescence and Photocatalytic Properties of Porous ZnO Nanosheets. *J. Mater.*

Chem. A **2014**, *2* (37), 15377–15388.

(85) Sahoo, P. K.; Kalyan Kamal, S. S.; Premkumar, M.; Jagadeesh Kumar, T.; Sreedhar, B.; Singh, A. K.; Srivastava, S. K.; Chandra Sekhar, K. Synthesis of Tungsten Nanoparticles by Solvothermal Decomposition of Tungsten Hexacarbonyl. *Int. J. Refract. Met. Hard Mater.* **2009**, *27* (4), 784–791.

(86) Patterson, A. L. The Scherrer Formula for X-Ray Particle Size Determination. *Phys. Rev.* **1939**, *56* (10), 978–982.

(87) Zhang, J.; Zhang, P.; Wang, T.; Gong, J. Monoclinic WO$_3$ Nanomultilayers with Preferentially Exposed (002) Facets for Photoelectrochemical Water Splitting. *Nano Energy* **2015**, *11*, 189–195.

(88) Yang, J.; Zhang, X.; Liu, H.; Wang, C.; Liu, S.; Sun, P.; Wang, L.; Liu, Y. Heterostructured TiO$_2$/WO$_3$ Porous Microspheres: Preparation, Characterization and Photocatalytic Properties. *Catal. Today* **2013**, *201*, 195–202.

(89) Konstantinou, I. K.; Albanis, T. A. TiO$_2$-Assisted Photocatalytic Degradation of Azo Dyes in Aqueous Solution: Kinetic and Mechanistic Investigations: A Review. *Appl. Catal. B Environ.* **2004**, *49* (1), 1–14.

(90) Konstantinou, I. K.; Albanis, T. A. Photocatalytic Transformation of Pesticides in Aqueous Titanium Dioxide Suspensions Using Artificial and Solar Light: Intermediates and Degradation Pathways. *Appl. Catal. B Environ.* **2003**, *42* (4), 319–335.

(91) Barakat, N. A. M.; Kanjwal, M. A.; Chronakis, I. S.; Kim, H. Y. Influence of Temperature on the Photodegradation Process Using Ag-Doped TiO$_2$ Nanostructures:

Negative Impact with the Nanofibers. *J. Mol. Catal. Chem.* **2013**, *366*, 333–340.

(92) Karimi, L.; Zohoori, S.; Yazdanshenas, M. E. Photocatalytic Degradation of Azo Dyes in Aqueous Solutions under UV Irradiation Using Nano-Strontium Titanate as the Nanophotocatalyst. *J. Saudi Chem. Soc.* **2014**, *18* (5), 581–588.

(93) Ball, D. W. Wien's Displacement Law as a Function of Frequency. *J. Chem. Educ.* **2013**, *90* (9), 1250–1252.

(94) Ghodsi, V.; Jin, S.; Byers, J. C.; Pan, Y.; Radovanovic, P. V. Anomalous Photocatalytic Activity of Nanocrystalline γ-Phase Ga_2O_3 Enabled by Long-Lived Defect Trap States. *J. Phys. Chem. C* **2017**, *121* (17), 9433–9441.

(95) Gnanaprakasam, A.; Sivakumar, V. M.; Thirumarimurugan, M. Influencing Parameters in the Photocatalytic Degradation of Organic Effluent via Nanometal Oxide Catalyst: A Review. *Indian J. Mater. Sci.* **2015**, *2015*, 601827.

(96) Zhou, D.; Wang, P.; Roy, C. R.; Barnes, M. D.; Kittilstved, K. R. Direct Evidence of Surface Charges in N-Type Al-Doped ZnO. *J. Phys. Chem. C* **2018**, *122* (32), 18596–18602.

(97) Yin, P.; Hegde, M.; Garnet, N. S.; Tan, Y.; Radovanovic, P. V. Faceting-Controlled Zeeman Splitting in Plasmonic TiO_2 Nanocrystals. *Nano Lett.* **2019**, *19* (9), 6695–6702.

(98) Wang, Y.; Zhao, X.; Duan, L.; Wang, F.; Niu, H.; Guo, W.; Ali, A. Structure, Luminescence and Photocatalytic Activity of Mg-Doped ZnO Nanoparticles Prepared by Auto Combustion Method. *Mater. Sci. Semicond. Process.* **2015**, *29*, 372–379.

(99) Li, Z.; Shen, W.; Xue, S.; Zu, X. Effect of Annealing Temperature on the Structural and

Optical Properties of Zn1−xMgxO Particles Prepared by Oxalate Precursor. *Colloids Surf. Physicochem. Eng. Asp.* **2008**, *320* (1), 156–160.

(100) Etacheri, V.; Roshan, R.; Kumar, V. Mg-Doped ZnO Nanoparticles for Efficient Sunlight-Driven Photocatalysis. *ACS Appl. Mater. Interfaces* **2012**, *4* (5), 2717–2725.